

Mesh adaptivity for quasi-static phase-field fractures based on a residual-type a posteriori error estimator

Katrin Mang¹, Mirjam Walloth², Thomas Wick¹, and Winnifried Wollner²

¹Leibniz Universität Hannover, Institut für Angewandte Mathematik,
AG Wissenschaftliches Rechnen, Welfengarten 1, 30167 Hannover, Germany

²Department of Mathematics, Technische Universität Darmstadt,
Dolivostrasse 15, 64293 Darmstadt, Germany

June 12, 2019

**This is the preprint version of an accepted article to be published in the
GAMM-Mitteilungen 2019**

<https://onlinelibrary.wiley.com/journal/15222608>

Abstract. In this work, we consider adaptive mesh refinement for a monolithic phase-field description for fractures in brittle materials. Our approach is based on an a posteriori error estimator for the phase-field variational inequality realizing the fracture irreversibility constraint. The key goal is the development of a reliable and efficient residual-type error estimator for the phase-field fracture model in each time-step. Based on this error estimator, error indicators for local mesh adaptivity are extracted. The proposed estimator is based on a technique known for singularly perturbed equations in combination with estimators for variational inequalities. These theoretical developments are used to formulate an adaptive mesh refinement algorithm. For the numerical solution, the fracture irreversibility is imposed using a Lagrange multiplier. The resulting saddle-point system has three unknowns: displacements, phase-field, and a Lagrange multiplier for the crack irreversibility. Several numerical experiments demonstrate our theoretical findings with the newly developed estimators and the corresponding refinement strategy.

1 Introduction

Fracture propagation and damage mechanics are current topics in theoretical mathematics (calculus of variations), numerical mathematics, and engineering. A well-established variational approach for

Griffith's [13] quasi-static brittle fracture was introduced by Francfort and Marigo [11]. The focus of the current work is on the development of a posteriori error estimation and local mesh adaptivity for such a variational (phase-field) fracture formulation.

Important motivations for mesh adaptivity are, first, the challenge of the resolution of the phase-field regularization parameter ϵ in relation to the spatial discretization parameter h such that $h \ll \epsilon$. Second, in many applications, the crack tip is of specific interest. Thus having an error estimator along with localized crack tip mesh refinement would be beneficial. We notice that mesh refinement for phase-field fracture problems may be problematic since it may occur that the (unknown) fracture path depends on the locally refined mesh. This yields numerical solutions purely dependent on the mesh refinement algorithm (see e.g., [5]) and discussions and references provided therein.

The first study on local mesh adaptivity for phase-field fracture was undertaken in [7]. An extension to anisotropic mesh adaptivity was done in [5]. Goal-oriented error estimation using dual-weighted residuals was addressed in [39]. Another method (only mesh refinement, but no error estimator) that purely focuses on fine meshes in the crack region has been developed in [16] for simulations in two spatial dimensions and the extension for three-dimensional computations was considered in [23]. Using these last developments, a computational convergence analysis using high performance parallel computing and local mesh adaptivity was carried out in [17]. All these studies show that local mesh refinement is a key ingredient for phase-field fractures, in particular in view of working with sufficiently small phase-field regularization parameters. However, due to the complexity of the problem setting such as nonlinearities and variational inequalities (due to the crack irreversibility constraint), further studies are necessary.

It has been observed, e.g., in [7], that asserting convergence in the individual residuals in each time step is sufficient to obtain stationary points of the phase-field problem. These residuals correspond to linear elasticity with a degenerated coefficient, and a singularly perturbed obstacle problem. Examples of linear elliptic problems with inequality constraints are obstacle and contact problems [30, 21]. Different types of error estimators for obstacle problems can be found in, e.g., [8, 38, 42]. By measuring the error in the solutions as well as in the constraining force, the first efficient and reliable residual-type estimator for obstacle problems has been derived in [31]. This approach has been extended to discontinuous Galerkin methods in [14, 15]. Error estimators for contact problems are given in [18, 37, 22]. In [26, 22] the local structure of the solution and constraining force has been exploited to localize the estimator contribution related to the constraints. This approach enables a good resolution of the critical regions between the phases of active and non-active constraints while avoiding over-refinement in the active set. An extension of this approach to discontinuous Galerkin methods has been used in [36].

The main contributions of this work are concerned with the development of an adaptive refinement strategy based on an a posteriori error estimator for the phase-field variational inequality, with particular emphasis on the robustness of the estimator with respect to the phase-field parameter ϵ . This aspect is a first difference to previous studies, in particular in comparison to [5] and [7] in which the irreversibility was modeled by enforcing zero values along the fracture and robustness of the estimator

was not considered. A second difference to previous works is that our adaptive refinement procedure will be based on consecutive solutions over the whole time interval on relatively coarse meshes, resulting in refinement indicators for the entire time horizon. These theoretical and algorithmic derivations are substantiated with appropriate numerical tests including studies with varying the relationship of the discretization parameter h and the crack width ϵ . In one numerical example, we are concerned with very fast crack growth in order to study whether the proposed estimator can cope with such situations.

The outline of this paper is as follows: In Section 2, we introduce the notation and our model formulation. Next, in Section 3, the discretization and the a posteriori error estimator for the phase-field variational inequality are developed. We complement this by providing the details for our numerical simulation in Section 4. In Section 5, some numerical tests are carried out for showing the performance of our theoretical developments (more details are provided in the last chapters at the end). We summarize our observations in Section 6.

2 Modeling

This section covers the basic notation, the function spaces, the required variables and the strong and weak problem formulation of a phase-field approach. We emanate from a two-dimensional, polygonal domain $\Omega \subset \mathbb{R}^2$. By means of an elliptic functional developed by Ambrosio-Tortorelli [2, 3] the lower-dimensional crack $C \subset \Omega$ is approximated by a phase-field variable $\varphi : (\Omega \times I) \rightarrow [0, 1]$ with $\varphi = 0$ in the crack and $\varphi = 1$ in the unbroken material. A parameter $\epsilon > 0$ determines the width of a transition zone between the unbroken material and the broken material inside the approximate crack.

Let I be a loading (time) interval $[0, T]$, where $T > 0$ is the end time value. A displacement function $\mathbf{u} : (\Omega \times I) \rightarrow \mathbb{R}^2$ is defined on the domain Ω . The boundary $\Gamma = \partial\Omega$ is a Dirichlet boundary for the displacements \mathbf{u} . For the phase-field variable, we have Neumann values $\nabla\varphi \cdot \mathbf{n} = 0$ on the whole boundary Γ where \mathbf{n} is the unit outward normal to the boundary. The physics of the underlying problem ask to enforce that the fracture cannot heal, i.e., that φ is monotone non-increasing with respect to $t \in I$. This condition is called irreversibility condition.

2.1 Strong formulation

In order to give the strong formulation of our model problem, we need some further definitions. The Frobenius scalar product of two matrices of the same dimension is denoted as $(\mathbf{A} : \mathbf{B}) := \sum_i \sum_j a_{ij} b_{ij}$.

A degradation function $g(\varphi)$ is defined as

$$g(\varphi) := (1 - \kappa)\varphi^2 + \kappa,$$

with a small regularization parameter $\kappa > 0$. The stress tensor $\boldsymbol{\sigma}(\mathbf{u})$ is given by

$$\boldsymbol{\sigma}(\mathbf{u}) := 2\mu \mathbf{E}_{\text{lin}}(\mathbf{u}) + \lambda \text{tr}(\mathbf{E}_{\text{lin}}(\mathbf{u}))\mathbf{I},$$

with the Lamé parameters $\mu, \lambda > 0$. Here, $\mathbf{E}_{\text{lin}}(\mathbf{u})$ is the linearized strain tensor:

$$\mathbf{E}_{\text{lin}}(\mathbf{u}) := \frac{1}{2}(\nabla\mathbf{u} + \nabla\mathbf{u}^T),$$

and \mathbf{I} denotes the two-dimensional identity matrix. In Miehe et al. [25] a stress splitting has been proposed for fracture phase-field models. The linearized strain tensor is decomposed into its tensile and compressive parts, i.e., $\mathbf{E}_{\text{lin}} := \mathbf{E}_{\text{lin}}^+ + \mathbf{E}_{\text{lin}}^-$ with

$$\mathbf{E}_{\text{lin}}^+ := \mathbf{Q}\mathbf{D}^+\mathbf{Q}^T,$$

where \mathbf{Q} is the matrix of eigenvectors and \mathbf{D} the matrix with the eigenvalues on the diagonal. Further, $(\cdot)^+$ denotes the positive part, i.e., on the diagonal of \mathbf{D}^+ are either the positive eigenvalues or zeros. We use the stress splitting of [25] which is given by

$$\begin{aligned}\boldsymbol{\sigma}^+(\mathbf{u}) &:= 2\mu \mathbf{E}_{\text{lin}}^+(\mathbf{u}) + \lambda \max\{0, \text{tr}(\mathbf{E}_{\text{lin}}(\mathbf{u}))\}\mathbf{I}, \\ \boldsymbol{\sigma}^-(\mathbf{u}) &:= 2\mu (\mathbf{E}_{\text{lin}}(\mathbf{u}) - \mathbf{E}_{\text{lin}}^+(\mathbf{u})) + \lambda (\text{tr}(\mathbf{E}_{\text{lin}}(\mathbf{u})) - \max\{0, \text{tr}(\mathbf{E}_{\text{lin}}(\mathbf{u}))\})\mathbf{I}.\end{aligned}$$

The continuous formulation attributed to Miehe et al. [25, 24] is given in the following. Find $\mathbf{u} : (\Omega \times I) \rightarrow \mathbb{R}^2$ and $\varphi : (\Omega \times I) \rightarrow \mathbb{R}$ such that

$$-\nabla \cdot (g(\varphi)\boldsymbol{\sigma}^+(\mathbf{u})) + \boldsymbol{\sigma}^-(\mathbf{u}) = 0 \quad \text{in } (\Omega \times I),$$

$$(1 - \kappa)\varphi\boldsymbol{\sigma}^+(\mathbf{u}) : \mathbf{E}_{\text{lin}}(\mathbf{u}) - \frac{G_c}{\epsilon}(1 - \varphi) + \epsilon G_c \Delta \varphi \geq 0 \quad \text{in } (\Omega \times I). \quad (1)$$

Herein, G_c is the critical energy release rate. The crack irreversibility condition is determined by

$$\partial_t \varphi \leq 0 \quad \text{in } (\Omega \times I), \quad (2)$$

which has to be cautiously treated in the numerical solution process.

The system is completed by continuous Dirichlet boundary conditions

$$\mathbf{u} = \mathbf{u}_D \quad \text{on } (\Gamma \times I),$$

for the displacement function \mathbf{u} , a complementarity relation between the phase-field equation in (1) and the crack irreversibility constraint in (2) as

$$\left((1 - \kappa)\varphi\boldsymbol{\sigma}^+(\mathbf{u}) : \mathbf{E}_{\text{lin}}(\mathbf{u}) - \frac{G_c}{\epsilon}(1 - \varphi) + \epsilon G_c \Delta \varphi \right) \cdot (\partial_t \varphi) = 0,$$

and an initial condition

$$\varphi(x, 0) = \varphi_0 \quad \text{in } (\Omega \times \{0\}).$$

2.2 Time-discrete weak formulation

From now on, we consider a time discrete formulation on a fixed subdivision $0 = t_0 < t_1 < \dots < t_N = T$ of the interval I . We define approximations $(\mathbf{u}^n, \varphi^n) \approx (\mathbf{u}(t_n), \varphi(t_n))$ and hence the irreversibility condition is given by $\varphi^n \leq \varphi^{n-1}$ for all $n = 1, \dots, N$.

For the formulation of the time step problems, we introduce the space $\mathcal{H} := \mathbf{H}^1(\Omega; \mathbb{R}^2)$ and let $\mathbf{u}_D^n = \mathbf{u}_D(t^n) \in \mathcal{H} \cap \mathcal{C}^0(\Gamma_D)$ be a continuation of the Dirichlet-data. For the displacement, we define

$\mathcal{H}_0 := \{\mathbf{w} \in \mathbf{H}^1(\Omega) \mid \mathbf{w} = \mathbf{0} \text{ a.e. on } \Gamma_D\}$, where $\mathbf{w} = \mathbf{0}$ on Γ_D has to be understood in the usual trace sense. The phase-field space is $\mathcal{H} = H^1(\Omega)$ with the feasible set $\mathcal{K}(\varphi^{n-1}) := \{\psi \in \mathcal{H} \mid \psi \leq \varphi^{n-1} \leq 1\}$.

In the following, we denote the L^2 -scalar product by $\langle \cdot, \cdot \rangle$ and the duality pairing of \mathcal{H} with its dual by $\langle \cdot, \cdot \rangle_{-1,1}$. For tensor-valued functions \mathbf{A} and \mathbf{B} , of the same dimensions, it holds $\langle \mathbf{A}, \mathbf{B} \rangle := \int_{\Omega} \mathbf{A} : \mathbf{B} \, dx$. The L^2 -norm is denoted by $\|\cdot\|$ and the H^1 -norm by $\|\cdot\|_1$.

Now, we can state the problem for calculating the solution $(\mathbf{u}^n, \varphi^n)$:

Problem 1 (Weak formulation in each time step). *For $n = 1, \dots, N$, and given φ^{n-1} , find $(\mathbf{u}^n, \varphi^n) \in (\mathcal{H}_0 + \{\mathbf{u}_D^n\}) \times \mathcal{K}(\varphi^{n-1})$ such that*

$$\begin{aligned} \langle g(\varphi^{n-1})\boldsymbol{\sigma}^+(\mathbf{u}^n), \mathbf{E}_{\text{lin}}(\mathbf{w}) \rangle + \langle \boldsymbol{\sigma}^-(\mathbf{u}^n), \mathbf{E}_{\text{lin}}(\mathbf{w}) \rangle &= 0 \quad \forall \mathbf{w} \in \mathcal{H}_0, \\ \langle (1 - \kappa)\varphi^n \boldsymbol{\sigma}^+(\mathbf{u}^n) : \mathbf{E}_{\text{lin}}(\mathbf{u}^n), \psi - \varphi^n \rangle - \frac{G_c}{\epsilon} \langle 1 - \varphi^n, \psi - \varphi^n \rangle & \\ + \epsilon G_c \langle \nabla \varphi^n, \nabla(\psi - \varphi^n) \rangle &\geq 0 \quad \forall \psi \in \mathcal{K}(\varphi^{n-1}). \end{aligned} \quad (3)$$

Remark 1. *In the first term we time-lag the phase-field variable in order to convexify the problem; see, e.g., [16].*

This proposed weak problem formulation is discretized in the following section.

3 Discretization and a posteriori error estimator

In this section, we first discuss the discretization in Section 3.1. Next, in Section 3.2 the residual-type error estimator for the variational inequality in the phase-field model is derived.

3.1 Discrete formulation

In the discrete setting, at each time step $n = 1, \dots, N$, we decompose the polygonal domain Ω by a (family of) meshes \mathfrak{M}^n consisting of shape regular parallelograms or triangles $\boldsymbol{\epsilon}$, such that all meshes share a common coarse mesh. To allow for local refinement, in particular of parallelogram elements, we allow for one hanging node per edge at which degrees of freedom will be eliminated to assert conformity of the discrete spaces. Further, we assume that the boundary of the domain is resolved by the chosen meshes.

To each mesh, we associate the mesh size function h^n , i.e., $h_{\boldsymbol{\epsilon}}^n = \text{diam } \boldsymbol{\epsilon}$ for any element $\boldsymbol{\epsilon} \in \mathfrak{M}^n$. The set of nodes p is given by \mathfrak{N} and we distinguish between the set \mathfrak{N}^{Γ} of nodes at the boundary and the set of interior nodes \mathfrak{N}^I .

Further, for a point $p \in \mathfrak{N}$, we define a patch ω_p as the interior of the union of all elements sharing the node p . We call the union of all sides in the interior of ω_p , not including the boundary of ω_p skeleton and denote it by γ_p^I . For boundary nodes, we denote the intersections between Γ and $\partial\omega_p$ by $\gamma_p^{\Gamma} := \Gamma \cap \partial\omega_p$. Further, we will make use of $\omega_{\mathfrak{s}}$ which is the union of all elements sharing a side \mathfrak{s} . Later on, we need the definition of the jump term $[\nabla\psi_h] := \nabla|_{\boldsymbol{\epsilon}}\psi_h \cdot \mathbf{n}_{\boldsymbol{\epsilon}} - \nabla|_{\tilde{\boldsymbol{\epsilon}}}\psi_h \cdot \mathbf{n}_{\tilde{\boldsymbol{\epsilon}}}$ where $\boldsymbol{\epsilon}, \tilde{\boldsymbol{\epsilon}}$ are neighboring elements and $\mathbf{n}_{\boldsymbol{\epsilon}}$ is the unit outward normal on the common side of the two elements.

For the discretization, we consider linear finite elements on triangles and bilinear finite elements on parallelograms. We abbreviate

$$\mathbb{S}_1(\boldsymbol{\epsilon}) := \begin{cases} \mathbb{P}_1(\boldsymbol{\epsilon}), & \text{if } \boldsymbol{\epsilon} \text{ is a triangle,} \\ \mathbb{Q}_1(\boldsymbol{\epsilon}), & \text{if } \boldsymbol{\epsilon} \text{ is a parallelogram.} \end{cases}$$

Thus, discrete solution spaces are given by

$$\mathcal{H}_h^n := \{\mathbf{v}_h \in \mathcal{C}^0(\bar{\Omega}; \mathbb{R}^2) \mid \forall \boldsymbol{\epsilon} \in \mathfrak{M}^n, \mathbf{v}_h|_{\boldsymbol{\epsilon}} \in \mathbb{S}_1(\boldsymbol{\epsilon})\} \subset \mathcal{H},$$

$$\mathcal{H}_{h,0}^n := \{\mathbf{v}_h \in \mathcal{H}_h^n \mid \mathbf{v}_h = \mathbf{0} \text{ on } \Gamma\} \subset \mathcal{H}_0,$$

$$\mathcal{H}_h^n := \{v_h \in \mathcal{C}^0(\bar{\Omega}) \mid \forall \boldsymbol{\epsilon} \in \mathfrak{M}^n, v_h|_{\boldsymbol{\epsilon}} \in \mathbb{S}_1(\boldsymbol{\epsilon})\} \subset \mathcal{H}.$$

We define the respective nodal interpolation operators as I_h^n , and define the discrete feasible set for the phase-field by

$$\mathcal{K}_h^n := \{\psi_h \in \mathcal{H}_h^n \mid \psi_h(p) \leq (I_h^n \varphi_h^{n-1})(p), \quad \forall p \in \mathfrak{N}\}.$$

The nodal basis functions of the finite element spaces \mathcal{H}_h^n are denoted by ϕ_p .

Analogous to Problem 1, we define the spatially discretized time step problem:

Problem 2 (Discrete formulation in each time step). *For $n = 1, \dots, N$ and φ^{n-1} given, find $(\mathbf{u}_h^n, \varphi_h^n) \in (\mathcal{H}_{h,0}^n + \{I_h^n \mathbf{u}_D^n\}) \times \mathcal{K}_h^n$ such that*

$$\begin{aligned} \langle g(I_h^n \varphi_h^{n-1}) \boldsymbol{\sigma}^+(\mathbf{u}_h^n), \mathbf{E}_{\text{lin}}(\mathbf{w}_h) \rangle + \langle \boldsymbol{\sigma}^-(\mathbf{u}_h^n), \mathbf{E}_{\text{lin}}(\mathbf{w}_h) \rangle &= 0 \quad \forall \mathbf{w}_h \in \mathcal{H}_{h,0}^n, \\ \langle (1 - \kappa) \varphi_h^n \boldsymbol{\sigma}^+(\mathbf{u}_h^n) : \mathbf{E}_{\text{lin}}(\mathbf{u}_h^n), \psi_h - \varphi_h^n \rangle - \frac{G_c}{\epsilon} \langle 1 - \varphi_h^n, \psi_h - \varphi_h^n \rangle & \\ + \epsilon G_c \langle \nabla \varphi_h^n, \nabla(\psi_h - \varphi_h^n) \rangle &\geq 0 \quad \forall \psi_h \in \mathcal{K}_h^n. \end{aligned} \quad (4)$$

3.2 Residual-type a posteriori estimator

In this section, we propose a residual-type a posteriori estimator for the variational inequality (4) in Problem 2. As the structure remains the same for all time steps, we consider exemplary one time step n . We drop the now superfluous superscript n , e.g., $\mathcal{H} := \mathcal{H}^n$, $\mathcal{H}_h := \mathcal{H}_h^n$ and $h_\epsilon := h_\epsilon^n$. With the bilinear form

$$a_{h,\epsilon}(\zeta, \psi) := \left\langle \left(\frac{G_c}{\epsilon} + (1 - \kappa) (\boldsymbol{\sigma}^+(\mathbf{u}_h^n) : \mathbf{E}_{\text{lin}}(\mathbf{u}_h^n)) \right) \zeta, \psi \right\rangle + G_c \epsilon \langle \nabla \zeta, \nabla \psi \rangle, \quad (5)$$

we abbreviate the discrete variational inequality in (4) by

$$a_{h,\epsilon}(\varphi_h, \psi_h - \varphi_h) \geq \left\langle \frac{G_c}{\epsilon}, \psi_h - \varphi_h \right\rangle \quad \forall \psi_h \in \mathcal{K}_h^n. \quad (6)$$

We define the corresponding discrete constraining force density $\Lambda_h \in \mathcal{H}_h^*$ as

$$\langle \Lambda_h, \psi_h \rangle_{-1,1} := \left\langle \frac{G_c}{\epsilon}, \psi_h \right\rangle - a_{h,\epsilon}(\varphi_h, \psi_h) \quad \forall \psi_h \in \mathcal{H}_h. \quad (7)$$

We note that the discrete constraining force Λ_h equals the linear residual $\mathcal{R}_h^{\text{lin}}$ for the corresponding unconstrained diffusion-reaction equations.

Further, with the bilinear form (5) and the admissible set $\mathcal{K}(I_h^n(\varphi_h^{n-1})) := \{\psi \in \mathcal{H} \mid \psi \leq I_h^n(\varphi_h^{n-1})\}$, we approximate the variational inequality in (3) by introducing an auxiliary variable $\hat{\varphi} \in \mathcal{K}(I_h^n(\varphi_h^{n-1}))$ solving

$$a_{h,\epsilon}(\hat{\varphi}, \psi - \hat{\varphi}) \geq \left\langle \frac{G_c}{\epsilon}, \psi - \hat{\varphi} \right\rangle \quad \forall \psi \in \mathcal{K}(I_h^n(\varphi_h^{n-1})). \quad (8)$$

Remark 2. As the bilinear form $a_{h,\epsilon}(\cdot, \cdot)$ depends on the approximation \mathbf{u}_h^n of \mathbf{u}^n and the constraints depend on the approximation $I_h^n(\varphi_h^{n-1})$ of φ^{n-1} , the solution $\hat{\varphi}$ of (8) is an approximation to the solution φ of (3).

It exists a distribution $\hat{\Lambda} \in \mathcal{H}^*$, called constraining force density, which turns the variational inequality (8) in an equation

$$\left\langle \hat{\Lambda}, \psi \right\rangle_{-1,1} := \left\langle \frac{G_c}{\epsilon}, \psi \right\rangle - a_{h,\epsilon}(\hat{\varphi}, \psi) \quad \forall \psi \in \mathcal{H}.$$

As the work [31] reveals that sharp a posteriori estimators for variational inequalities can be derived by involving the error in the constraining forces, we measure the error in the solution of (8) as well as in the constraining forces. Similar to [35], we measure the error of the solution of (8) in the energy norm

$$\|\cdot\|_\epsilon := \left\{ G_c \epsilon \|\nabla(\cdot)\|^2 + \left\| \left(\frac{G_c}{\epsilon} + (1 - \kappa) \boldsymbol{\sigma}^+(\mathbf{u}_h^n) : \mathbf{E}_{\text{lin}}(\mathbf{u}_h^n) \right)^{\frac{1}{2}} (\cdot) \right\|^2 \right\}^{\frac{1}{2}},$$

corresponding to the bilinear form $a_{h,\epsilon}(\cdot, \cdot)$. The error in the constraining forces is measured in the corresponding dual norm

$$\|\cdot\|_{*,\epsilon} := \frac{\sup_{\psi \in \mathcal{H}^1} \langle \cdot, \psi \rangle}{\|\psi\|_\epsilon}.$$

In order to compare the continuous and discrete constraining forces, we cannot use Λ_h , as by definition (7) it is a functional on the space of discrete functions and there is no unique extension to \mathcal{H}^* . Therefore, we need to choose an extension which is a discrete counterpart of $\hat{\Lambda}$ as functional on H^1 , reflecting the properties of the constraining force and depending on the discrete solution and given data. We call this extension quasi-discrete constraining force and denote it by $\tilde{\Lambda}_h$.

In [31], an extension to a functional on H^1 was proposed by means of lumping $\sum_{p \in \mathfrak{N}^C} s_p \phi_p$, where

$$s_p = \frac{\langle \Lambda_h, \phi_p \rangle_{-1,1}}{\int_{\omega_p} \phi_p \, dx} \geq 0 \quad (9)$$

are the node values of the lumped discrete constraining force. This approach has been extended and applied to different obstacle and contact problems in, e.g., [27, 26, 22, 14, 15, 36, 34, 35].

Following the works [26, 35], we distinguish between full-contact nodes $p \in \mathfrak{N}^{fC}$ and semi-contact nodes $p \in \mathfrak{N}^{sC}$. Full-contact nodes are those nodes for which the solution is fixed to the obstacle $\varphi_h = I_h^n \varphi_h^{n-1}$ on ω_p and the sign condition

$$\left\langle \mathcal{R}_h^{\text{lin}}, \varphi \right\rangle_{-1,1,\omega_p} \geq 0 \quad \forall \varphi \geq 0 \in H_0^1(\omega_p)$$

is fulfilled. The latter condition means that the solution is locally not improvable, see the explanation in [26]. Semi-contact nodes are those nodes for which $\varphi_h(p) = I_h^n \varphi_h^{n-1}(p)$ holds but not the conditions of full-contact. Based on this classification, we define the quasi-discrete constraining force as

$$\langle \tilde{\Lambda}_h, \psi \rangle_{-1,1} := \sum_{p \in \mathfrak{N}^{sC}} \langle \tilde{\Lambda}_h^p, \psi \phi_p \rangle_{-1,1} + \sum_{p \in \mathfrak{N}^{fC}} \langle \tilde{\Lambda}_h^p, \psi \phi_p \rangle_{-1,1}. \quad (10)$$

For the definition of the local contributions, we shorten the element residual with

$$r(\varphi_h) := \frac{G_c}{\epsilon} + G_c \epsilon \Delta \varphi_h - \frac{G_c}{\epsilon} \varphi_h - (1 - \kappa)(\boldsymbol{\sigma}^+(\mathbf{u}_h^n) : \mathbf{E}_{\text{lin}}(\mathbf{u}_h^n)) \varphi_h.$$

For semi-contact nodes, we consider the following local contribution in (10)

$$\langle \tilde{\Lambda}_h^p, \psi \phi_p \rangle_{-1,1} = \int_{\gamma_p^I} G_c \epsilon [\nabla \varphi_h] c_p(\psi) \phi_p \, dx + \int_{\omega_p} r(\varphi_h) c_p(\psi) \phi_p \, dx,$$

with $c_p(\psi) = \frac{\int_{\tilde{\omega}_p} \psi \phi_p \, dx}{\int_{\tilde{\omega}_p} \phi_p \, dx}$, where $\tilde{\omega}_p$ is the patch around p with respect to two uniform red-refinements.

For full-contact nodes we define the following local contribution in (10) as

$$\langle \tilde{\Lambda}_h^p, \psi \phi_p \rangle_{-1,1} := \int_{\gamma_p^I} G_c \epsilon^2 [\nabla \varphi_h] \psi \phi_p \, dx + \int_{\omega_p} r(\varphi_h) \psi \phi_p \, dx.$$

With these definitions, we define the error measure

$$\|\hat{\varphi} - \varphi_h\|_\epsilon + \|\hat{\Lambda} - \tilde{\Lambda}_h\|_{*,\epsilon}. \quad (11)$$

In order to state the error estimator

$$\eta := \sum_{k=1}^4 \eta_k \quad (12)$$

for the error measure (11), we define for each node p

$$\alpha_p := \min_{x \in \omega_p} \left\{ \frac{G_c}{\epsilon} + (1 - \kappa)(\boldsymbol{\sigma}^+(\mathbf{u}_h^n) : \mathbf{E}_{\text{lin}}(\mathbf{u}_h^n)) \right\},$$

and $h_p := \text{diam}(\omega_p)$. The local contributions are

$$\begin{aligned} \eta_1 &:= \left(\sum_{p \in \mathfrak{N} \setminus \mathfrak{N}^{fC}} \eta_{1,p}^2 \right)^{\frac{1}{2}}, & \eta_{1,p} &:= \min \left\{ \frac{h_p}{\sqrt{G_c \epsilon}}, \alpha_p^{-\frac{1}{2}} \right\} \|r(\varphi_h)\|_{\omega_p}, \\ \eta_2 &:= \left(\sum_{p \in \mathfrak{N}^I \setminus \mathfrak{N}^{fC}} \eta_{2,p}^2 \right)^{\frac{1}{2}}, & \eta_{2,p} &:= \min \left\{ \frac{h_p}{\sqrt{G_c \epsilon}}, \alpha_p^{-\frac{1}{2}} \right\}^{\frac{1}{2}} (G_c \epsilon)^{-\frac{1}{4}} \|G_c \epsilon [\nabla \varphi_h]\|_{\gamma_p^I}, \\ \eta_3 &:= \left(\sum_{p \in \mathfrak{N}^\Gamma \setminus \mathfrak{N}^{fC}} \eta_{3,p}^2 \right)^{\frac{1}{2}}, & \eta_{3,p} &:= \min \left\{ \frac{h_p}{\sqrt{G_c \epsilon}}, \alpha_p^{-\frac{1}{2}} \right\}^{\frac{1}{2}} (G_c \epsilon)^{-\frac{1}{4}} \|G_c \epsilon \nabla \varphi_h\|_{\gamma_p^\Gamma}, \\ \eta_4 &:= \left(\sum_{p \in \mathfrak{N}^{sC}} \eta_{4,p}^2 \right)^{\frac{1}{2}}, & \eta_{4,p} &:= \left(s_p \int_{\tilde{\omega}_p} (I_h^n \varphi_h^{n-1} - \varphi_h) \phi_p \, dx \right)^{\frac{1}{2}}. \end{aligned}$$

We emphasize that the estimator contributions related to the constraints are localized to the area of semi-contact and no contributions arise from full-contact nodes.

Under the assumption that φ_h is a linear finite element function, we will prove in a forthcoming publication that η constitutes global upper and local lower bounds of (11). The estimator η provides a robust upper bound where robust means that the constant in the bound does not depend on ϵ such that the validity of the estimator holds for arbitrary choices of ϵ .

Theorem 1. Reliability of the error estimator

The error estimator η (12) provides a robust upper bound of the error measure (11):

$$\|\hat{\varphi} - \varphi_h\|_\epsilon + \|\hat{\Lambda} - \tilde{\Lambda}_h\|_{*,\epsilon} \lesssim \eta.$$

The local lower bounds are summarized in the following Theorems.

Theorem 2. Local lower bounds by $\eta_{1,p}, \eta_{2,p}, \eta_{3,p}$

The error estimator contributions $\eta_{k,p}$, $k = 1, 2, 3$ constitute the following robust local lower bounds

$$\eta_{k,p} \lesssim \|\hat{\varphi} - \varphi_h\|_{\epsilon, \omega_p} + \|\hat{\Lambda} - \tilde{\Lambda}_h\|_{*, \epsilon, \omega_p}.$$

Theorem 3. Local lower bound by $\eta_{4,p}$

For nodes $p \in \mathfrak{N}^{sC}$ with $\frac{h_p}{\sqrt{G_c \epsilon}} \leq \alpha_p^{-\frac{1}{2}}$ we have the robust local lower bound

$$\begin{aligned} \eta_{4,p} \lesssim & \|\hat{\varphi} - \varphi_h\|_{\epsilon, \omega_p} + \|\hat{\Lambda} - \tilde{\Lambda}_h\|_{*, \epsilon, \omega_p} \\ & + \min \left\{ \frac{h_p}{\sqrt{G_c \epsilon}}, \alpha_p^{-\frac{1}{2}} \right\}^{\frac{1}{2}} (G_c \epsilon)^{-\frac{1}{4}} \|G_c \epsilon [\nabla(I_h^n \varphi_h^{n-1} - \varphi_h)]^I\|_{\gamma_p}. \end{aligned} \quad (13)$$

Otherwise, for nodes $p \in \mathfrak{N}^{sC}$ with $\alpha_p^{-\frac{1}{2}} < \frac{h_p}{\sqrt{G_c \epsilon}}$ we have the local lower bound

$$\begin{aligned} \eta_{4,p} \lesssim & \|\hat{\varphi} - \varphi_h\|_{\epsilon, \omega_p} + \|\hat{\Lambda} - \tilde{\Lambda}_h\|_{*, \epsilon, \omega_p} \\ & + \alpha_p^{\frac{3}{4}} (G_c \epsilon)^{-\frac{3}{4}} \min \left\{ \frac{h_p}{\sqrt{G_c \epsilon}}, \alpha_p^{-\frac{1}{2}} \right\}^{\frac{1}{2}} (G_c \epsilon)^{-\frac{1}{4}} \|G_c \epsilon [\nabla(I_h^n \varphi_h^{n-1} - \varphi_h)]^I\|_{\gamma_p}. \end{aligned} \quad (14)$$

Remark 3. We note that the additional term in the bound (13) only occurs for $p \in \mathfrak{N}^{sC}$ and is of the same order as the other estimator contributions. In the application, we expect the semi-contact zone to be well resolved, especially with respect to ϵ such that $\frac{h_p}{\sqrt{G_c \epsilon}} \leq \alpha_p^{-\frac{1}{2}}$ after a finite number of adaptive refinement steps such that the local lower bound is robust everywhere.

Remark 4. In this work, we focus on the novel estimator for the phase-field inequality to obtain a good resolution of the fracture growth. We therefore only provide a residual-type a posteriori estimator for the variational inequality in Problem 2. For the equation in the coupled system of Problem 2, a standard a posteriori estimator [32] could be applied.

4 Solver and refinement strategy

The numerical solution proceeds from Problem 2. Concerning the robustness, efficiency and the accuracy of the coupling terms, we made good experiences treating the phase-field system in a monolithic fashion, e.g., [40, 41]. At first, the handling of the crack irreversibility constraint is clarified. In the following section, the spatial discretization and the overall solution method are explained.

4.1 Solution algorithms

In order to compute a discrete approximation of the solution of the quasi-static fracture phase-field model, we use a semi-smooth Newton method [19] implemented in [12]. The semi-smooth Newton method is based on the following complementarity system which is equivalent to the variational inequality system of Problem 1.

It is easy to see, that by introducing a Lagrange multiplier $\Lambda^n \in \mathcal{H}^*$ [20, 29, 33] the weak formulation (3), in the continuous setting, is equivalent to the complementarity system: given $n = 1, \dots, N$ and φ^{n-1} to find $(\mathbf{u}^n, \varphi^n, \Lambda^n) \in (\mathcal{H}_0 + \{\mathbf{u}_D^n\}) \times \mathcal{K}(\varphi^{n-1}) \times \mathcal{H}^*$ satisfying

$$\begin{aligned} \langle g(\varphi^{n-1})\boldsymbol{\sigma}^+(\mathbf{u}^n), \mathbf{E}_{\text{lin}}(\mathbf{w}) \rangle + \langle \boldsymbol{\sigma}^-(\mathbf{u}^n), \mathbf{E}_{\text{lin}}(\mathbf{w}) \rangle &= 0 & \forall \mathbf{w} \in \mathcal{H}_0, \\ \langle (1 - \kappa)\varphi^n \boldsymbol{\sigma}^+(\mathbf{u}^n) : \mathbf{E}_{\text{lin}}(\mathbf{u}^n), \psi \rangle - \frac{G_c}{\epsilon} \langle 1 - \varphi^n, \psi \rangle \\ + \epsilon G_c \langle \nabla \varphi^n, \nabla \psi \rangle + \langle \Lambda^n, \psi \rangle_{-1,1} &= 0 & \forall \psi \in \mathcal{H}, \\ \langle \Lambda^n, \psi \rangle_{-1,1} &\geq 0, & \forall \psi \in \mathcal{H}, \psi \geq 0, \\ \varphi^n &\leq \varphi^{n-1}, \\ \langle \Lambda^n, \varphi^{n-1} - \varphi^n \rangle_{-1,1} &= 0. \end{aligned}$$

To obtain the complementarity formulation for the discretization (4), we define $(\mathcal{H}_h^n)^*$ by a dual basis of \mathcal{H}_h^n ; i.e., we let $(\mathcal{H}_h^n)^* = \text{span}\{\phi_p^* \mid p \in \mathfrak{N}\}$, where

$$\langle \phi_p^*, \phi_q \rangle = \delta_{pq}$$

for the nodal basis ϕ_q of \mathcal{H}_h^n . Then, we define $\Lambda_h^n = \sum_{p \in \mathfrak{N}} (\Lambda_h^n)_p \phi_p^*$ by setting

$$\langle \Lambda_h^n, \phi_p \rangle = - \langle (1 - \kappa)\varphi_h^n \boldsymbol{\sigma}^+(\mathbf{u}_h^n) : \mathbf{E}_{\text{lin}}(\mathbf{u}_h^n), \phi_p \rangle + \frac{G_c}{\epsilon} \langle 1 - \varphi_h^n, \phi_p \rangle - \epsilon G_c \langle \nabla \varphi_h^n, \nabla \phi_p \rangle$$

for all $p \in \mathfrak{N}$. This immediately gives the analogous discrete complementarity system

$$\begin{aligned} \langle g(I_h^n \varphi_h^{n-1})\boldsymbol{\sigma}^+(\mathbf{u}_h^n), \mathbf{E}_{\text{lin}}(\mathbf{w}_h) \rangle + \langle \boldsymbol{\sigma}^-(\mathbf{u}_h^n), \mathbf{E}_{\text{lin}}(\mathbf{w}_h) \rangle &= 0 & \forall \mathbf{w}_h \in \mathcal{H}_{h,0}^n, \\ \langle (1 - \kappa)\varphi_h^n \boldsymbol{\sigma}^+(\mathbf{u}_h^n) : \mathbf{E}_{\text{lin}}(\mathbf{u}_h^n), \psi_h \rangle - \frac{G_c}{\epsilon} \langle 1 - \varphi_h^n, \psi_h \rangle \\ + \epsilon G_c \langle \nabla \varphi_h^n, \nabla \psi_h \rangle + \langle \Lambda_h^n, \psi_h \rangle &= 0 & \forall \psi_h \in \mathcal{H}_h^n, \\ \langle \Lambda_h^n, \phi_p \rangle &\geq 0, & \forall p \in \mathfrak{N}, \\ \varphi_h^n(p) &\leq \varphi_h^{n-1}(p), & \forall p \in \mathfrak{N}, \\ \langle \Lambda_h^n, I_h^n \varphi_h^{n-1} - \varphi_h^n \rangle &= 0. \end{aligned} \tag{15}$$

Remark 5. We recall that the discrete variational inequality (6) for which we derived the a posteriori estimator in Section 3.2 is part of the discrete phase-field model (Problem 2). Due to the equivalence of Problem 2 and the complementarity system (15) it holds that $\langle \Lambda_h, \phi_p \rangle_{-1,1}$ in (15) and (7) are the same. The only difference is that now we have chosen a discrete basis for Λ_h such that the node value $(\Lambda_h^n)_p$ equals $s_p \cdot \int_{\omega_p} \phi_p \, dx$ in (9).

To apply a semi-smooth Newton method, we notice, that by choice of the basis the complementarity conditions are equivalent to the following complementarity system for the coefficients $\varphi^n(p)$ and $(\Lambda_h^n)_p$:

$$\begin{aligned} (\Lambda_h^n)_p &= \langle \Lambda_h^n, \phi_p \rangle \geq 0, & \forall p \in \mathfrak{N}, \\ \varphi^n(p) &\leq \varphi^{n-1}(p), & \forall p \in \mathfrak{N}, \\ \sum_{p \in \mathfrak{N}} (\Lambda_h^n)_p (I_h^n \varphi^{n-1} - \varphi^n)(p) &= \langle \Lambda_h^n, I_h^n \varphi^{n-1} - \varphi^n \rangle = 0. \end{aligned}$$

Using the complementarity function $(x, y) \mapsto x - \max(0, x + cy)$, for arbitrary $c > 0$, we can equivalently express (15) as the system

$$\begin{aligned} \langle g(I_h \varphi_h^{n-1}) \boldsymbol{\sigma}^+(\mathbf{u}_h^n), \mathbf{E}_{\text{lin}}(\mathbf{w}_h) \rangle + \langle \boldsymbol{\sigma}^-(\mathbf{u}_h^n), \mathbf{E}_{\text{lin}}(\mathbf{w}_h) \rangle &= 0 & \forall \mathbf{w}_h \in \mathcal{H}_{h,0}^n, \\ \langle (1 - \kappa) \varphi_h^n \boldsymbol{\sigma}^+(\mathbf{u}_h^n) : \mathbf{E}_{\text{lin}}(\mathbf{u}_h^n), \psi_h \rangle - \frac{G_c}{\epsilon} \langle 1 - \varphi_h^n, \psi_h \rangle & \\ + \epsilon G_c \langle \nabla \varphi_h^n, \nabla \psi_h \rangle + \langle \Lambda_h^n, \psi_h \rangle_{-1,1} &= 0 & \forall \psi_h \in \mathcal{H}_h^n, \\ (\Lambda_h^n)_p - \max(0, (\Lambda_h^n)_p + c((I_h^n \varphi^{n-1} - \varphi^n)(p))) &= 0, & \forall p \in \mathfrak{N}. \end{aligned} \tag{16}$$

Now, a time step n can be reformulated, using (16), as given φ_h^{n-1} :

Find $U_h^n := U_h = (u_h, \varphi_h, \Lambda_h) \in \mathcal{U}_h + \{\mathbf{u}_D^n\} := ((\mathcal{H}_{h,0} + \{\mathbf{u}_D^n\}) \times \mathcal{H}_h \times \mathcal{H}_h^*)$, such that

$$A(U_h) = 0$$

abbreviating (16). To solve this non-linear equation, we formulate a residual-based Newton scheme utilizing that the max operator is semi-smooth in finite dimensions.

To measure the residuals and monitoring functions, we use the discrete norm $\|\cdot\| := \|\cdot\|_{l^\infty}$ measuring the maximal absolute value of the coordinate vectors. At a given time instance t_n , we shall find the loading step solution U_h^n using:

Algorithm 1 (Residual-based Newton's method). *Choose $\rho \in (0, 1)$ and an initial Newton guess $U^{(0)} \in \mathcal{U}_h + \{\mathbf{u}_D^n\}$. Typically, $U^{(0)} = I_h^n U_h^{n-1}$ up to a correction for the Dirichlet-values.*

For the iteration steps $k = 0, 1, 2, 3, \dots$:

1. *Stop, if converged and return $U_h^n = U^{(k)}$.*

2. *Find $\delta U^{(k)} \in \mathcal{U}_h$ such that*

$$A'(U^{(k)})(\delta U^{(k)}) = -A(U^{(k)}).$$

3. *Find a maximal $s_k \in \{\rho^l \mid l \in 0, \dots, 1\}$ such that*

$$\|A(U^{(k)} + s_k \delta U^{(k)})\| < \|A(U^{(k)})\|.$$

4. *Set*

$$U^{(k+1)} = U^{(k)} + s_k \delta U^{(k)}.$$

For computational reasons, several of the steps need to be slightly modified, e.g., by only reassembling the matrix if the convergence rate is too slow, and for simplicity the linear systems in the Newton algorithm are solved by UMFPAK [9]. For details, we refer to our implementation in [10, 12].

4.2 Refinement strategy

The used adaptive solution strategy is given in this section. The mesh adaptation is realized using extracted local error indicators from the a posteriori error estimator (12) on the given meshes over all time steps.

This information is used to adapt the mesh using the following strategy:

Algorithm 2. *Given a time discretization $t_0 < \dots < t_N$, and an initial mesh $\mathfrak{M}^n = \mathfrak{M}$ for all $n = 0, \dots, N$.*

1. *Set $\varphi_h^0 = I_h^0 \varphi^0$ and solve the discrete complementarity system (16) to obtain the discrete solutions $\mathbf{u}_h^n, \varphi_h^n, \Lambda_h^n$ for all $n = 1, \dots, N$.*
2. *Evaluate the error estimator (12) in order to obtain η^n for each time step.*
3. *Stop, if $\sum_{n=1}^N (\eta^n)^2$ and $\|I_h^n \varphi^{n-1} - \varphi^{n-1}\|$ are small enough for all $n = 1, \dots, N$.*
4. *For each $n = 1, \dots, N$, mark elements in \mathfrak{M}^n based on η^n according to an optimization strategy, as implemented in deal.II [4]. This strategy allows to flag certain cells to reach a grid that is optimal with respect to an objective function that tries to balance reducing the error and increasing the numerical cost. More details on this approach can be found in [28].*
5. *Refine the meshes according to the marking, and satisfaction of the constraints on hanging nodes.*
6. *Repeat from step 1.*

5 Numerical tests

In this section, we study the quality of the error estimator proposed in Section 3.2. For that, we use two crack propagation settings in pure elasticity regimes (each with three studies resulting in a total of six scenarios). The following questions and aspects are addressed:

- Does the error estimator allow to resolve the mushy zone around the crack sufficiently? (Both Studies in Section 5.2 and 5.3)
- How does adaptive mesh refinement performs in comparison to uniform mesh refinement in terms of the convergence of the, so-called, load-displacement curves? (Study 1 in Section 5.2)
- Investigating the $\epsilon - h$ relationship (Study 2 in Section 5.3)
- Observing the error indicators and the corresponding adaptively refined meshes (Study 3 in Section 5.4).

The implementation is done in the open-source package Differential Equations and Optimization Environment library (DOpElib) [10, 12] using the finite elements from deal.II [4].

In the simulations, we declare a strip of size $4h_{\text{start}}$ below the top boundary to be ignored by the estimator. Thus, we avoid that the error estimator resolves the singularity due to the non-matching boundary conditions which allow for a fracture to form directly below the top-boundary.

5.1 Configurations

The two numerical configurations are set according to [24]: the single edge notched shear test and the single edge notched tension test, the boundary-values are selected according to [41]. Both tests were used by several groups with similar settings and it is well known that under constant tension the crack grows in a straight line, while under constant shear forces the crack grows in a curve towards a corner [6, 24, 16, 1].

5.1.1 The single edge notched shear test

The geometry and the material parameters of the single edge notched shear test are adopted from [24] and displayed in Figure 1. Here, the domain Ω is a two-dimensional square of 10 mm length with a given crack (called slit) on the right side at 5 mm tending to the midpoint of the square. On the bottom boundary the square is fixed, on the top boundary a given force in x -direction pulls to the left. We follow the boundary conditions described in [41].

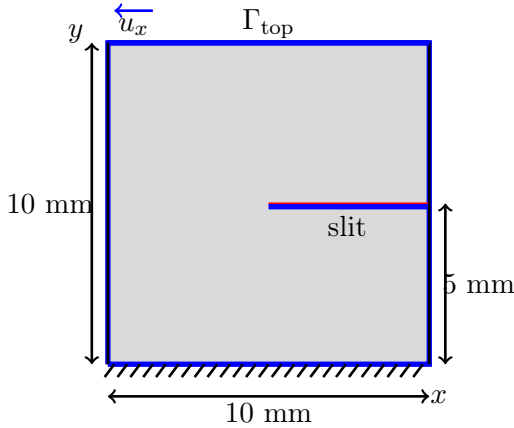


Figure 1: **(Single edge notched shear test)**

Geometry and boundary conditions. On the left and right side and the lower part of the slit, the boundary condition in y -direction is $u_y = 0$ mm and traction-free in x -direction. On the bottom boundary it holds $u_x = u_y = 0$ mm. On the top boundary, it holds $u_y = 0$ mm and in x -direction we determine a time-dependent non-homogeneous Dirichlet condition: $u_x = t \cdot 1$ mm/s with $0 \leq t \leq 0.0125$ s with a time step size $\delta t > 0$.

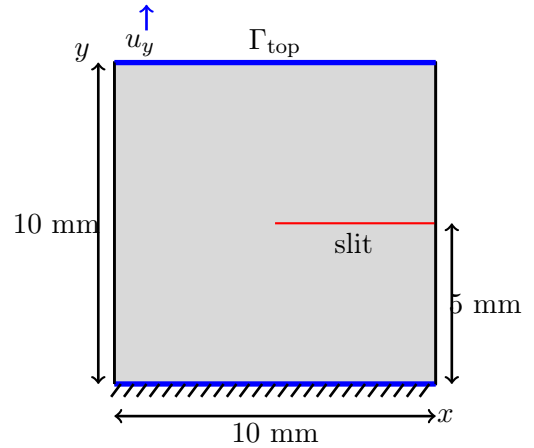


Figure 2: **(Single edge notched tension test)**

Geometry and boundary conditions. On the left and right side, the boundaries are traction-free (homogeneous Neumann condition). On the bottom boundary it holds $u_y = 0$ mm. On the top boundary, it holds $u_x = 0$ mm and in y -direction we determine a time-dependent non-homogeneous Dirichlet condition: $u_y = t \cdot 1$ mm/s with $0 \leq t \leq 0.00676$ s with a time step size $\delta t > 0$.

The material and model parameters are given as follows: the Lamé coefficients are given as $\lambda = 121.15$ kN/mm² and $\mu = 80.77$ kN/mm². The critical energy release rate G_c is defined as $G_c = 2.7$ N/mm. The loading increment is chosen as $\delta t = 10^{-4}$ s and the bulk regularization parameter $\kappa = 10^{-10}$ is sufficiently small. The mesh element diameter is set as $h_{\text{start}} = 0.088$ mm. The end time T is 0.0125 s, once the specimen is fully cracked.

5.1.2 The single edge notched tension test

The geometry and the material parameters are in line with the single edge notched shear test in the previous section. The only difference is in the boundary conditions. As depicted in Figure 2, it is pulled with a given force in y -direction on the top boundary and the bottom boundary is fixed in y -direction. Also most of the numerical parameters are chosen as in the single edge notched shear test in Section 5.1.1. Here, the mesh element diameter is set as $h_{\text{start}} = 0.044$ mm. In this setting, we use as loading increment $\delta t = 10^{-5}$ s, which is necessary because of a very fast crack growth. The end time T is 0.00676 s, once the specimen is fully cracked.

5.1.3 Quantities of Interest

For both tests and all three studies, we discuss proper quantities of interest. In the first and second study we observe the load-displacement curves, where the load functions on the top boundary Γ_{top} are computed by

$$\boldsymbol{\tau} = (F_x, F_y) := \int_{\Gamma_{\text{top}}} \boldsymbol{\sigma}(\mathbf{u}_h) \mathbf{n} \, ds, \quad (17)$$

with the stress tensor $\boldsymbol{\sigma}(\mathbf{u}_h)$ and the normal vector \mathbf{n} . In the load-displacement curves the loading is displayed versus the displacements. Within the single edge notched shear test we are particularly interested in the loading force F_x , within the tension test we are interested in the evaluation of F_y .

As a second quantity of interest, the bulk energy E_b is defined as

$$E_b := \int_{\Omega} \left(([1 - \kappa]\varphi^2 + \kappa) \mu \operatorname{tr} (E_{\text{lin}}(\mathbf{u}_h))^2 + \frac{1}{2} \lambda \operatorname{tr} (E_{\text{lin}}(\mathbf{u}_h))^2 \right) dx. \quad (18)$$

Further the crack energy is computed via

$$E_c := \frac{G_C}{2} \int_{\Omega} \left(\frac{(\varphi - 1)^2}{\epsilon} + \epsilon |\nabla \varphi|^2 \right) dx. \quad (19)$$

In addition, especially in Study 3, we show snapshots of the phase-field function and the current adaptive mesh at certain time steps.

5.2 Study 1: uniform versus adaptive refinement

In a first study, the focus is on the comparison of adaptive meshes and a uniformly refined mesh. We compare the results of the load-displacement curves, the bulk and the crack energy after one to six steps of adaptive refinement starting with a coarser mesh than the used uniform refined mesh for a fair comparison. First, the results of the single edge notched shear test are given. For all tests executed in Study 1, the relation between the discretization parameter h_{start} and ϵ is given by $\epsilon = 2h_{\text{start}}$ which means that we refine in h , but not in ϵ . The cell length h_{start} is chosen as in the previous test.

5.2.1 Results of the single edge notched shear test

In the following, the load-displacement curves, the bulk and crack energy will be given for seven conducted numerical tests. For the adaptive tests (named *adaptive* + number of refinement steps),

the coarsest mesh is pre-refined three times, while the uniform computation is done on a mesh with six levels of global refinement. In Figure 3, seven load-displacement curves are plotted. The loading F_x is computed as defined in (17). In Figure 4 the corresponding maximal number of degrees of freedom, at each time step, are given for each test. The tests called *adaptive* 1 to 6 show the load-displacement curves computed on an adaptive mesh based on a certain number of refinement cycles (one to six) according to Algorithm 2. The uniform mesh consists of 66,820 degrees of freedom (6 uniform refinement steps, $h = 0.011$ mm), which exceeds by far the number of degrees of freedom of the adaptive mesh after six steps of refinement based on the developed error estimator.

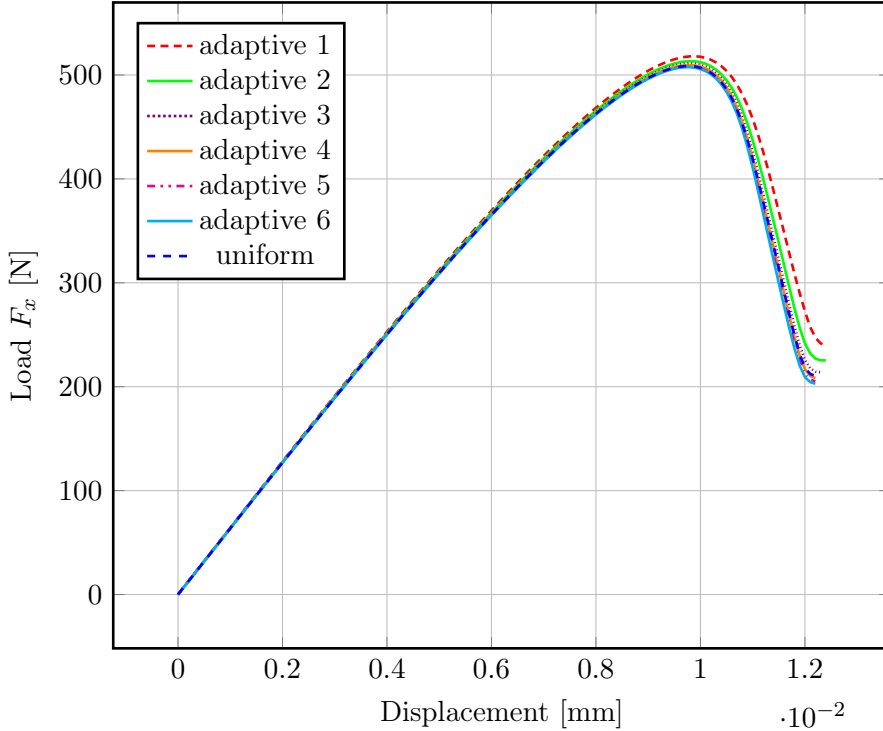


Figure 3: Load-displacement curves for the single edge notched shear test with six steps of uniform refinement compared to six steps of adaptive refinement and three steps of pre-refinement. We fix $\epsilon = 2h_{\text{start}}$ with h_{start} as the discretization length on the coarsest mesh. It means, ϵ is fixed while h decreases over the adaptive refinement steps.

In Figure 3, with only 18,196 degrees of freedom (test *adaptive* 6) we obtain nearly the same load-displacement curve as on the uniform refined mesh with 66,820 degrees of freedom. Furthermore, with an increasing number of refinement steps, we observe convergence towards the load-displacement curve computed with uniform mesh refinement.

We continue with the quantities bulk energy (defined in Equation (18)) and crack energy (defined in Equation (19)) with the same test setup as listed in Figure 4. Notice that neither the load in Figure 3 nor the bulk-energy 5 vanish at the end of the loading process. This is due to the fact, cf. [1], that the chosen stress-splitting does not allow for complete fracture.

Comparing the results of the bulk and crack energy depicted in the Figures 5 and 6, we observe that, once crack propagation starts, the bulk energy decreases and the crack energy increases. Secondly, similar to the load-displacement curves the course of the bulk and crack energy over time/loading tends

| Test name | # DoFs |
|------------|--------|
| adaptive 1 | 2,672 |
| adaptive 2 | 3,928 |
| adaptive 3 | 9,836 |
| adaptive 4 | 12,740 |
| adaptive 5 | 16,024 |
| adaptive 6 | 18,196 |
| uniform | 66,820 |

Figure 4: Maximal number of degrees of freedom for each test case for Study 1 designed for the single edge notched shear test.

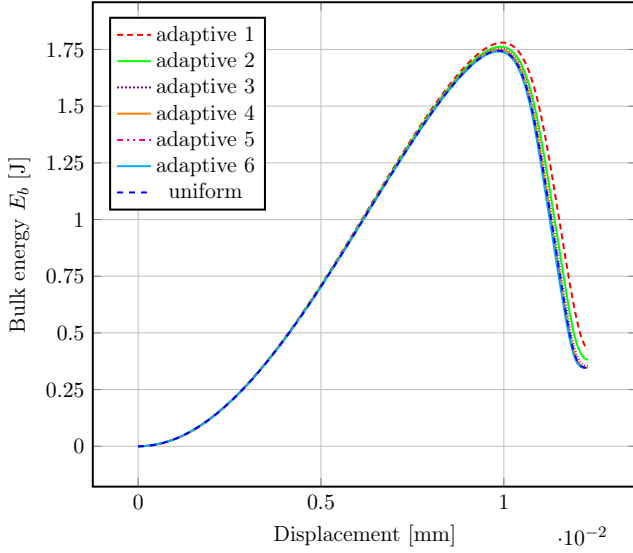


Figure 5: Bulk energy for the single edge notched shear test with six steps of uniform refinement compared to six steps of adaptive refinement and three steps of pre-refinement. We fix $\epsilon = 2h_{\text{start}}$, while h decreases over the adaptive refinement steps.

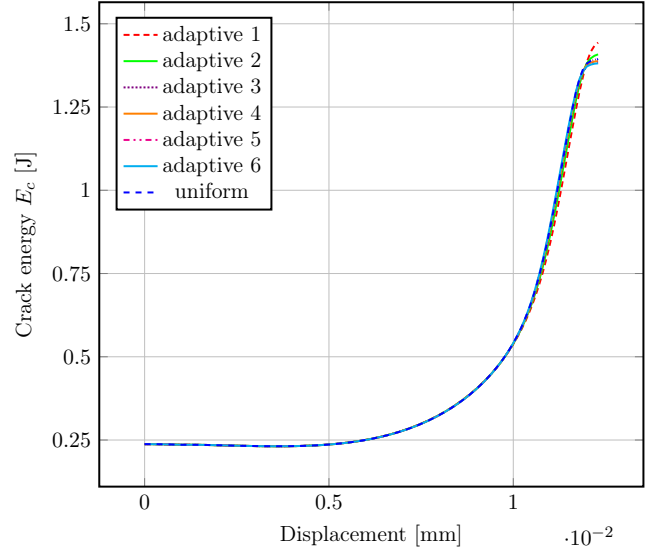


Figure 6: Crack energy for the single edge notched shear test with six steps of uniform refinement compared to six steps of adaptive refinement and three steps of pre-refinement. We fix $\epsilon = 2h_{\text{start}}$, while h decreases over the adaptive refinement steps.

towards the curves given by the computation on a uniformly refined mesh with an increasing number of refinement steps.

5.2.2 Results of the single edge notched tension test

In the following, the load-displacement curves, the bulk and the crack energy are computed and presented for six conducted numerical tests based on the tension test. For this test, the coarsest mesh is pre-refined four times, while the uniform computation is done as in the shear test on a mesh with six levels of global refinement.

In Figure 7, six load-displacement curves are plotted. In Figure 4, the corresponding maximal number of degrees of freedom are given for each test. As in the shear example, the tests called *adaptive* 1 to 5 show the load-displacement curves (loading F_y computed via (17)) based on an adaptive mesh with a certain number of refinement steps (1 to 5). The uniform mesh consists of 66,820 degrees of freedom (6 uniform refinement steps, $h = 0.011$ mm), which is more than the adaptive mesh after five steps of refinement based on the developed error estimator. Comparing the test based on a uniform mesh and the one with three adaptive refinement steps (dotted violet curve in Figure 7), the load-displacement curves are quite similar, although the adaptive test computes with maximal 18,408 degrees of freedom per time step.

As already discussed for the single edge notched shear test, the evolution of the bulk and crack energy visualized in the Figures 9 and 10 is of the expected behavior: as long as the crack does not grow, only the bulk energy increases. After crack propagation, bulk energy is dissipated into crack energy.

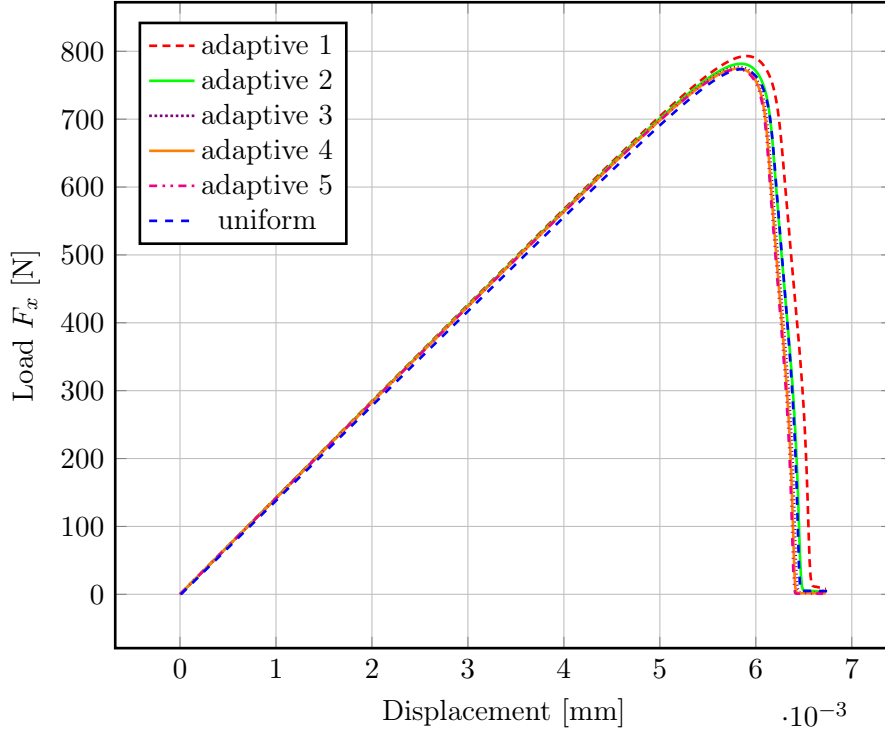


Figure 7: Load-displacement curves for the single edge notched tension test with six steps of uniform refinement compared to five steps of adaptive refinement and four steps of pre-refinement. We fix $\epsilon = 2h_{\text{start}}$, while h decreases over the adaptive refinement steps.

| Test name | # DoFs |
|------------|--------|
| adaptive 1 | 6,468 |
| adaptive 2 | 11,052 |
| adaptive 3 | 18,408 |
| adaptive 4 | 37,916 |
| adaptive 5 | 61,704 |
| uniform | 66,820 |

Figure 8: Maximal number of degrees of freedom for each test case for Study 1 designed for the single edge notched tension test.

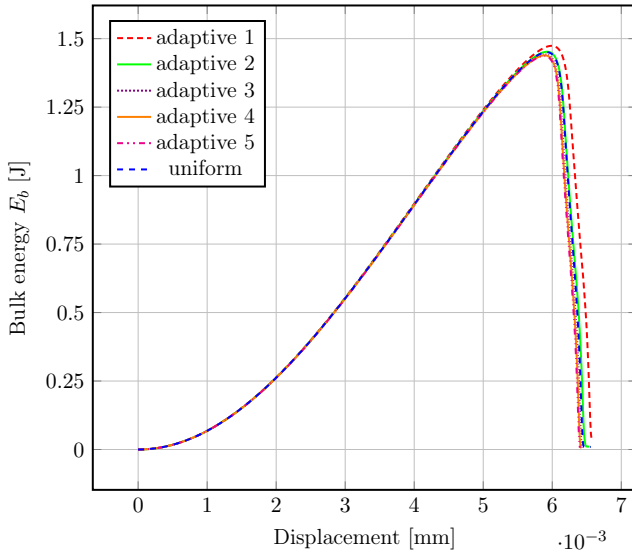


Figure 9: Bulk energy for the single edge notched tension test with six steps of uniform refinement compared to five steps of adaptive refinement and four steps of pre-refinement. We fix $\epsilon = 2h_{\text{start}}$, while h decreases over the adaptive refinement steps.

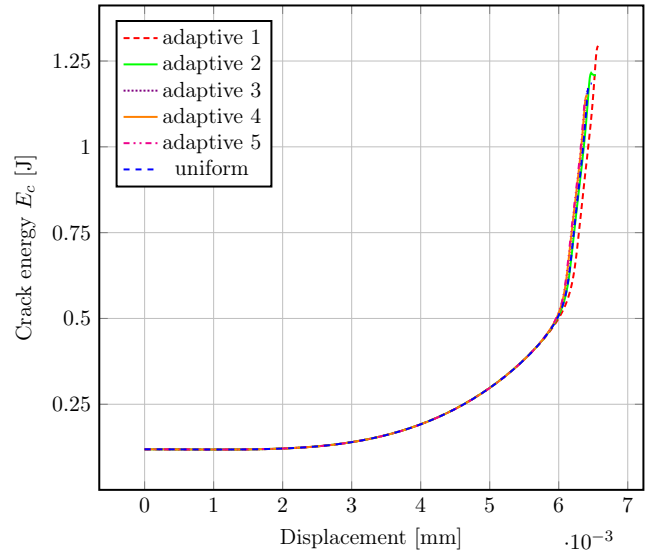


Figure 10: Crack energy for the single edge notched tension test with six steps of uniform refinement compared to five steps of adaptive refinement and four steps of pre-refinement. We fix $\epsilon = 2h_{\text{start}}$, while h decreases over the adaptive refinement steps.

5.3 Study 2: $\epsilon - h$ relationship

Now, we are interested in the numerical results of tests with different relations of the discretization parameter h_{start} on the initial mesh and the crack bandwidth ϵ . We investigate the $h_{\text{start}} - \epsilon$ relationship as follows:

- Case 1: $\epsilon = 2h_{\text{start}}$ with a fixed discretization parameter $h_{\text{start}} = 0.088$ mm, while h is decreasing during increasing refinement steps
- Case 2: $\epsilon = h_{\text{start}}$ with $h_{\text{start}} = 0.088$ mm fixed during refinement
- Case 3: $\epsilon = \frac{1}{2}h_{\text{start}}$ with $h_{\text{start}} = 0.088$ mm fixed during refinement

5.3.1 Results of the single edge notched shear test

In Figure 11, the load-displacement curves are depicted for the three test cases mentioned above. For all load-displacement curves one can observe convergence, even if for $\epsilon \geq h_{\text{start}}$, the results are more precise and more similar to the one in Figure 3.

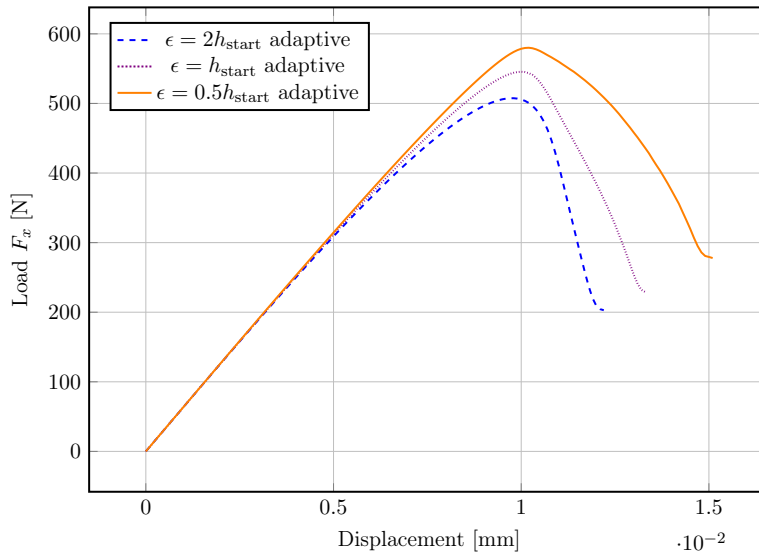


Figure 11: Load-displacement curves for the single edge notched shear test with three steps of global pre-refinement and six steps of adaptive refinement and $\epsilon = 2h_{\text{start}}$, $\epsilon = h_{\text{start}}$ and $\epsilon = 0.5h_{\text{start}}$.

The same can be observed for the bulk and crack energy in the Figures 12 and 13. The general course of the energies is acceptable, but with a decreasing bandwidth ϵ , the curves are less accurate against the starting point of crack propagation. Similar observations were made in [16].

5.3.2 Results of the single edge notched tension test

As expected, the load-displacement curves in Figure 14 for the three test cases $\epsilon = 2h_{\text{start}}$, $\epsilon = h_{\text{start}}$ and $\epsilon = 0.5h_{\text{start}}$ show an increase of the loading with an increasing displacement and a steep descent at the point where the crack starts propagating. For $\epsilon = 0.5h_{\text{start}}$ apparently the transition zone can be resolved sufficiently after five steps of adaptive refinement based on the initial mesh. This behavior can be recognized in the plotted energies in the Figures 15 and 16.

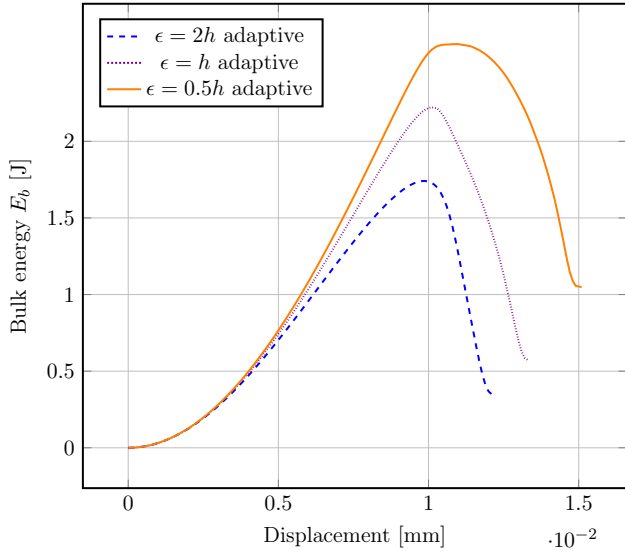


Figure 12: Bulk energy for the single edge notched shear test with three steps of global pre-refinement and six steps of adaptive refinement and $\epsilon = 2h_{\text{start}}$, $\epsilon = h_{\text{start}}$ and $\epsilon = 0.5h_{\text{start}}$.

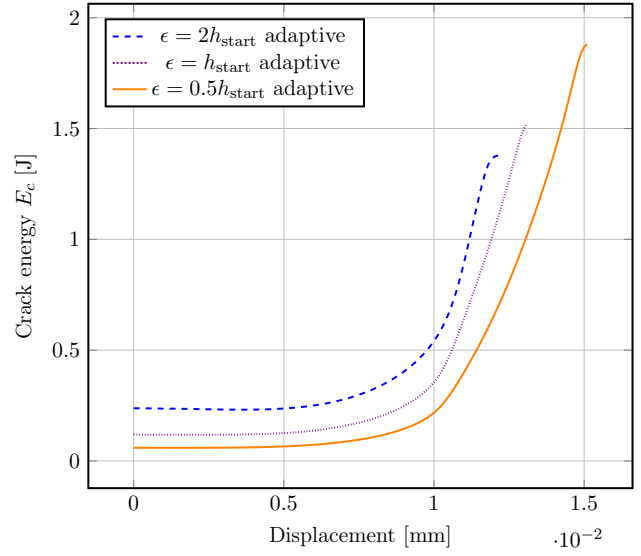


Figure 13: Crack energy for the single edge notched shear test with three steps of global pre-refinement and six steps of adaptive refinement and $\epsilon = 2h_{\text{start}}$, $\epsilon = h_{\text{start}}$ and $\epsilon = 0.5h_{\text{start}}$.

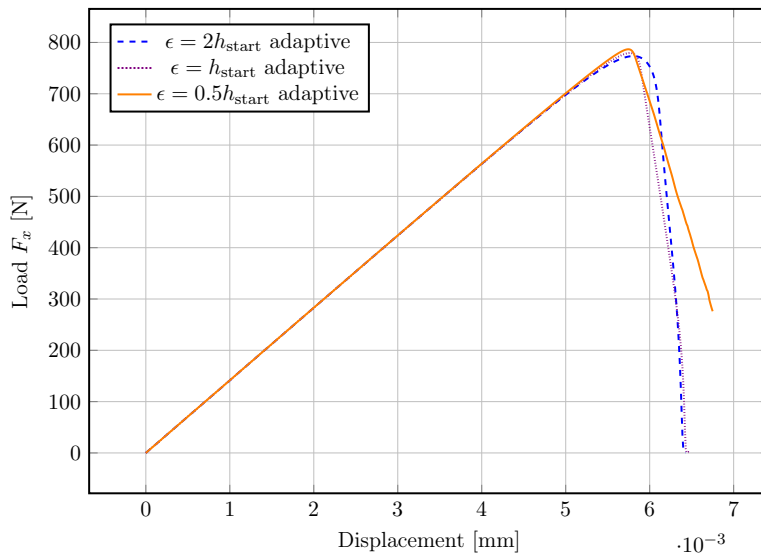


Figure 14: Load-displacement curves for the single edge notched tension test with four steps of global pre-refinement and five steps of adaptive refinement and $\epsilon = 2h_{\text{start}}$, $\epsilon = h_{\text{start}}$ and $\epsilon = 0.5h_{\text{start}}$.

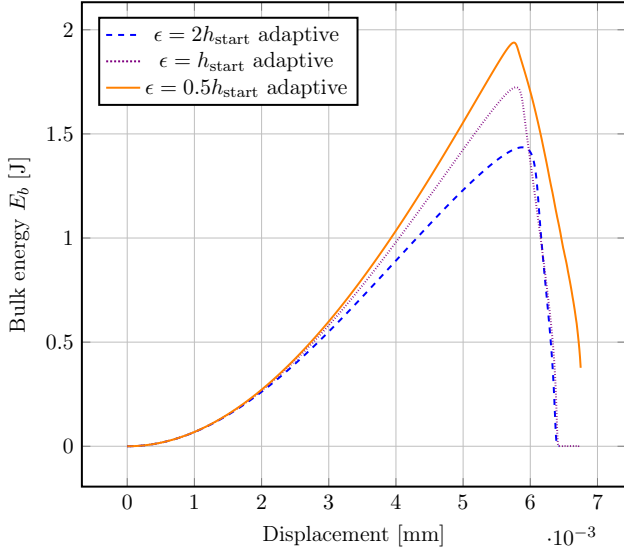


Figure 15: Bulk energy for the single edge notched tension test with four steps of global pre-refinement and five steps of adaptive refinement and $\epsilon = 2h_{\text{start}}$, $\epsilon = h_{\text{start}}$ and $\epsilon = 0.5h_{\text{start}}$.

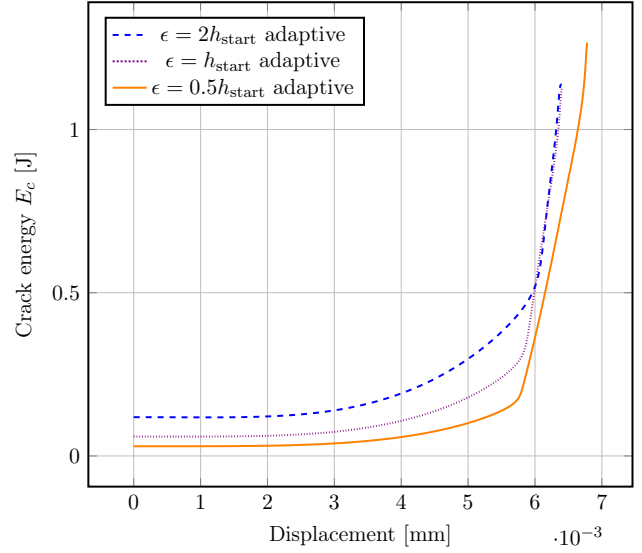


Figure 16: Crack energy for the single edge notched tension test with four steps of global pre-refinement and five steps of adaptive refinement and $\epsilon = 2h_{\text{start}}$, $\epsilon = h_{\text{start}}$ and $\epsilon = 0.5h_{\text{start}}$.

The results in Section 5.3, in particular $\epsilon = 0.5h_{\text{start}}$, indicate that our adaptive algorithm performs well even if the relation $\epsilon > 2h_{\text{start}}$ is not satisfied as it is required on uniform meshes for a reasonable accuracy of the crack approximation, cf. [25, Figure 4].

5.4 Study 3: adaptive meshes and local error indicators

In this final study, we present snapshots of the adaptively refined meshes and provide visualizations of the local error indicators.

5.4.1 Results of the single edge notched shear test

In Figure 17 and Figure 18, the phase-field function is depicted after 115, 119 and 125 time steps, respectively. The course of the crack to the left lower corner is as expected and as it can be found in the literature, e.g., [24, 6, 16, 1].

The snapshots in the first row in Figure 17 and Figure 18 indicate, that the error estimation and the corresponding refinement strategy allow to impress the zone around the crack after three refinement steps; in particular after six steps of adaptive refinement.

Further, the snapshots in Figure 19 allow to see the adaptive mesh especially in the crack domain enlarged in the time steps 116 and 125. Mesh cells far away of the fracture are unrefined or very coarse in contrast to the close region of the fracture.

5.4.2 Results of the single edge notched tension test

For the single edge notched tension test, in Figure 20 and Figure 21 the phase-field function is displayed after 615, 635 and 676 time steps. The course of the crack to the left boundary is as expected and in line with the literature, e.g., [24, 16].

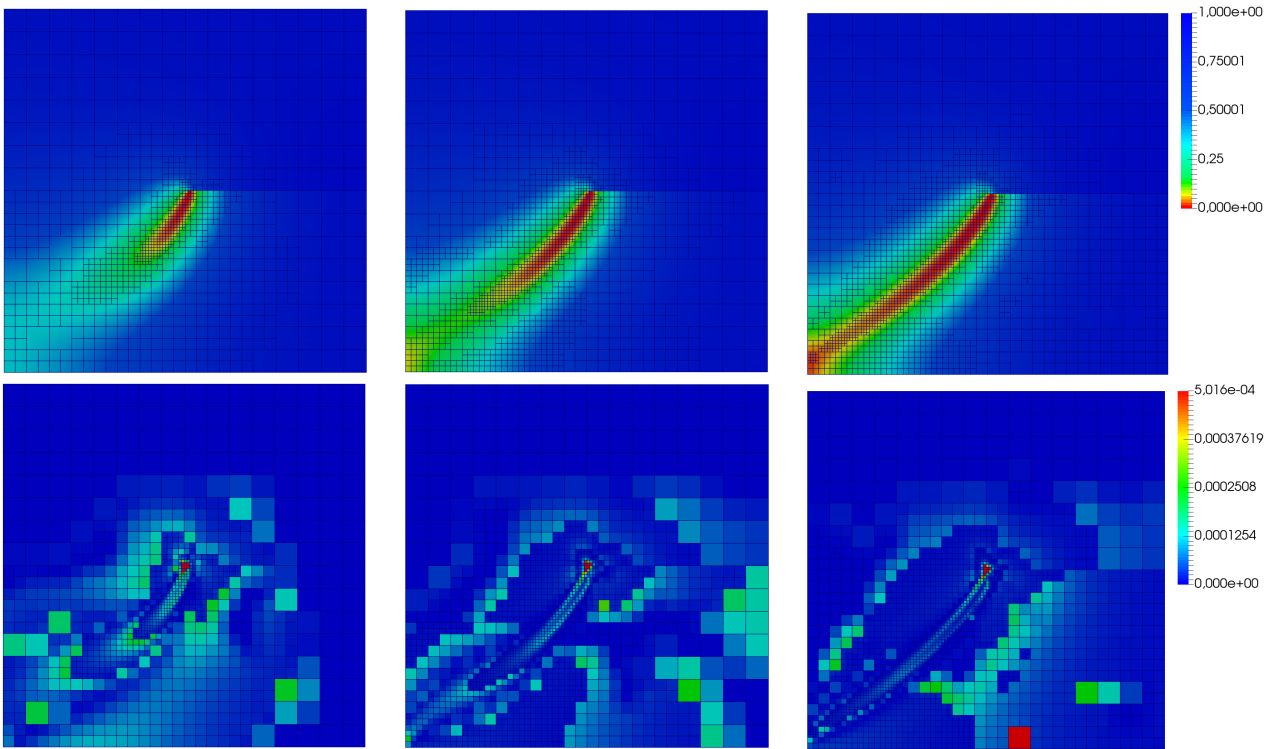


Figure 17: The phase-field function and the error indicators, respectively, after three refinement steps given in certain time steps (after 0.0115, 0.00119 and 0.00125 s) for the single edge notched shear test given on the current adaptive mesh to visualize the refinement strategy.

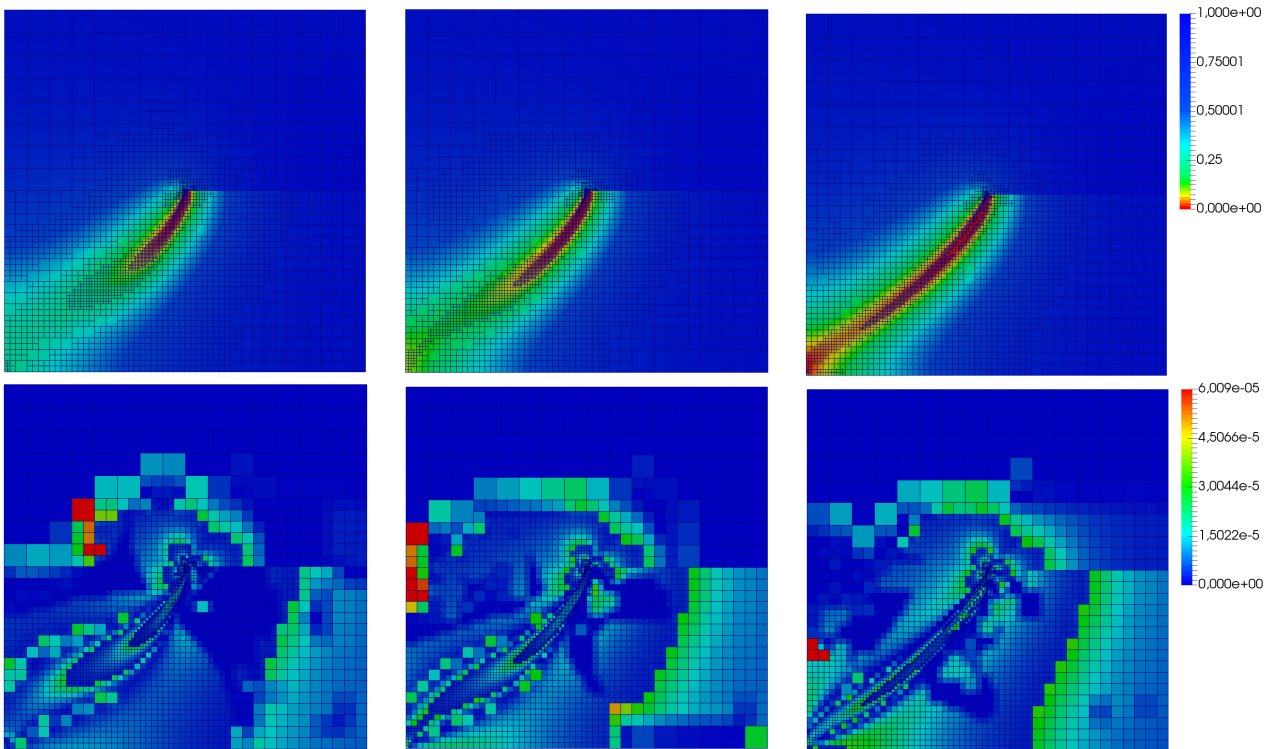


Figure 18: The phase-field function and the error indicators, respectively, after six refinement steps depicted in certain time steps (after 0.0116, 0.0118 and 0.0125 s) for the single edge notched shear test given on the current adaptive mesh to visualize the refinement strategy.

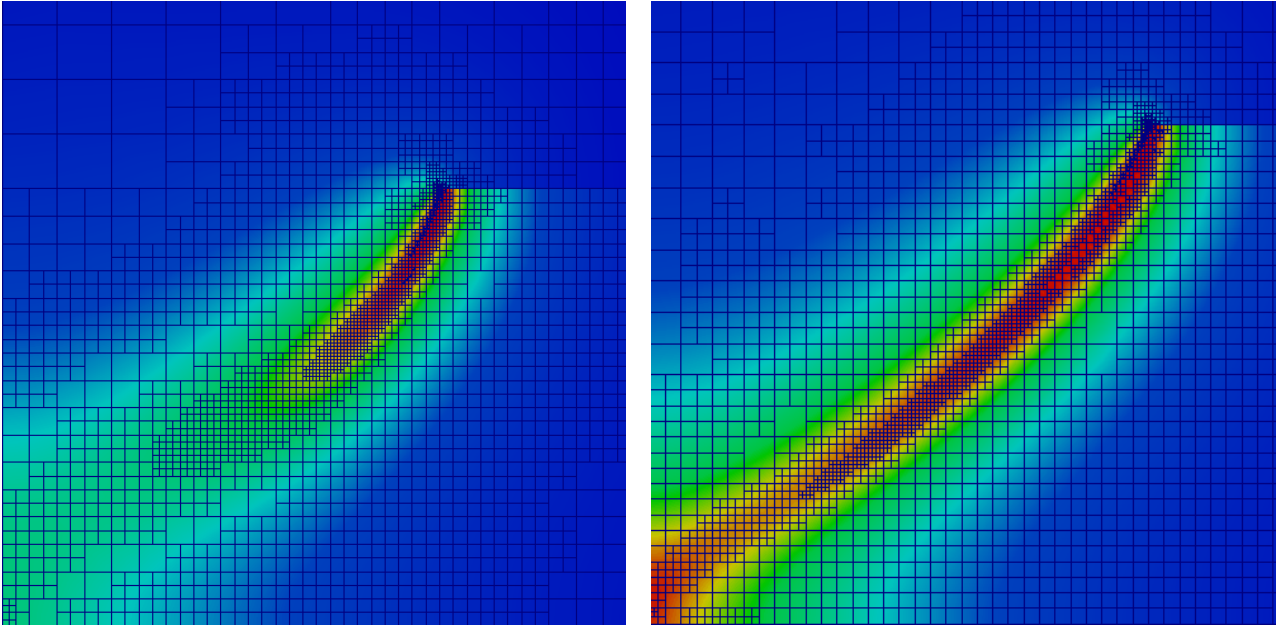


Figure 19: Enhanced extract of the phase-field function after six refinement steps in two certain time steps (after 0.0116 and 0.0125 s) for the single edge notched shear test given on the current adaptive mesh.

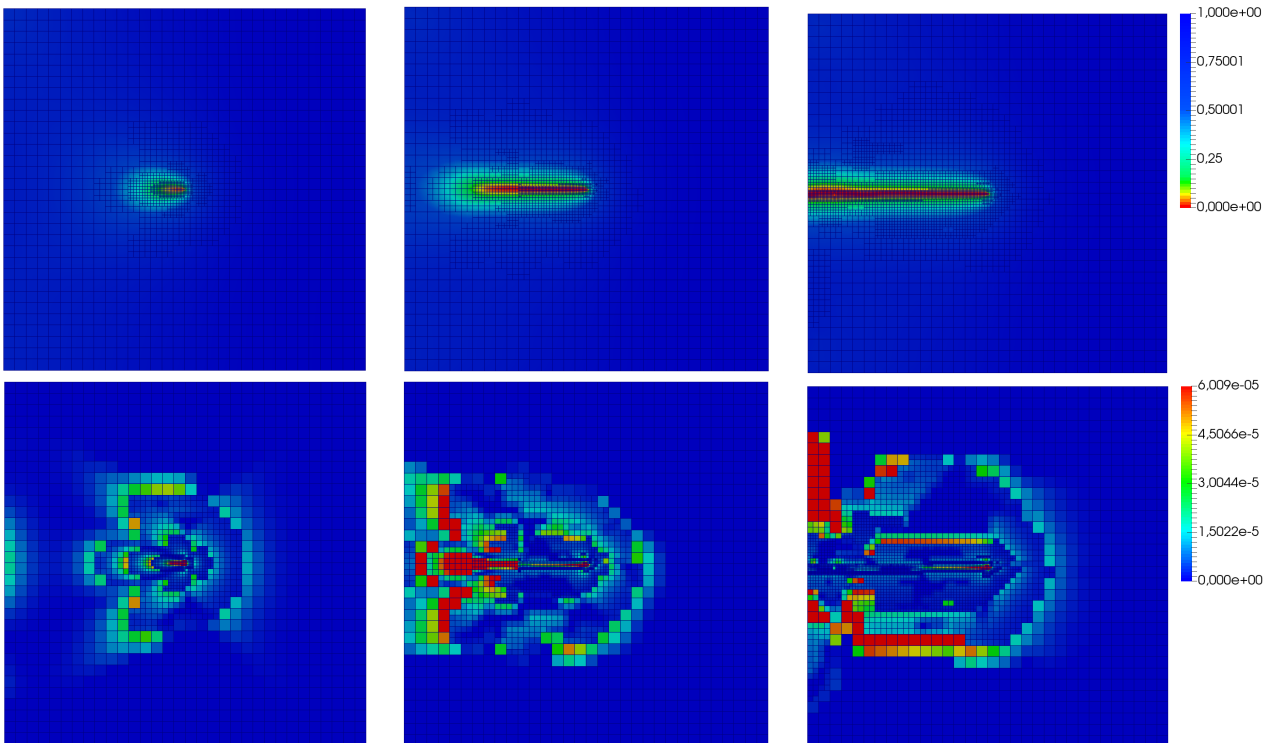


Figure 20: The phase-field function and the error indicators, respectively, after three refinement steps in certain time steps (after 0.00615, 0.00635 and 0.00676 s) for the single edge notched tension test given on the current adaptive mesh to visualize the refinement strategy.

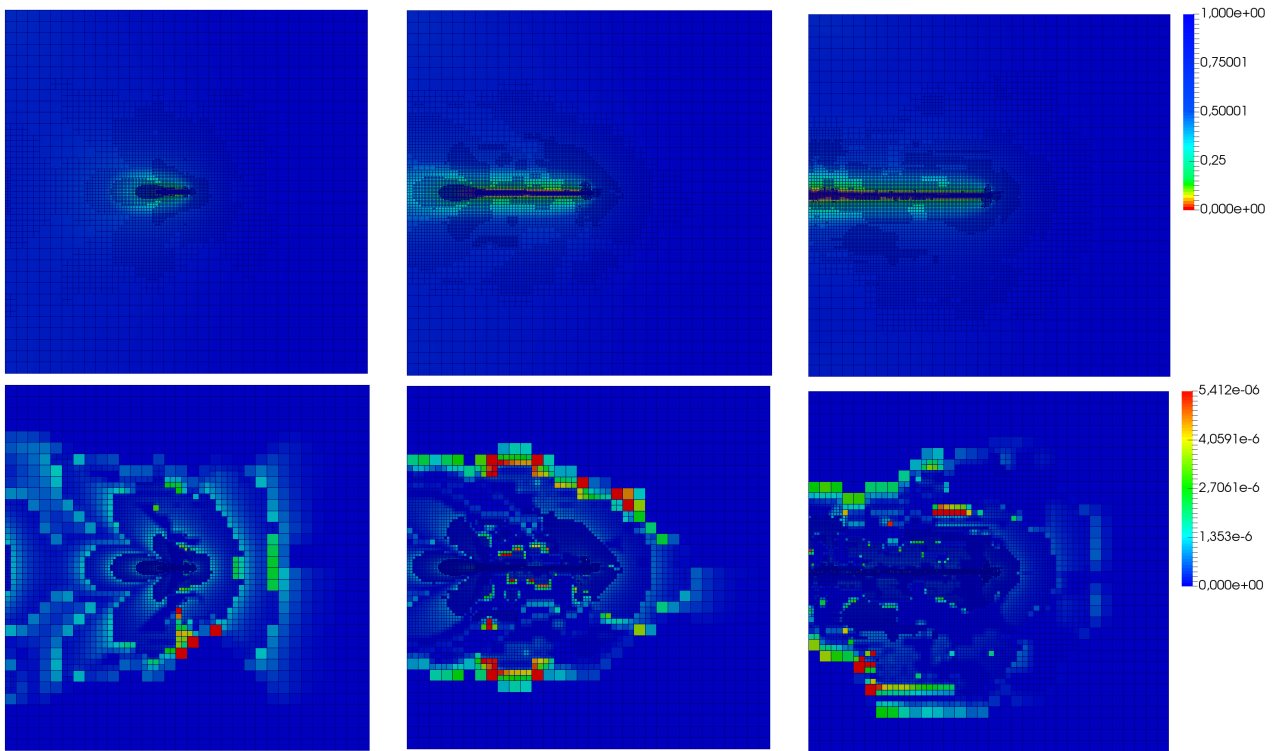


Figure 21: The phase-field function and the error indicators, respectively, after six refinement steps in certain time steps (after 0.00615, 0.00635 and 0.00674 s) for the single edge notched tension test given on the current adaptive mesh to visualize the refinement strategy.

In the Figures 20 and 21, we observe within the fast crack propagation of the tension test, that the error estimator marks cells with high errors especially in the region before the crack tip, which secures, that the crack itself moves in a refined region. Further, the plotted error indicators show the symmetry of this test in comparison to the non-symmetric shear test.

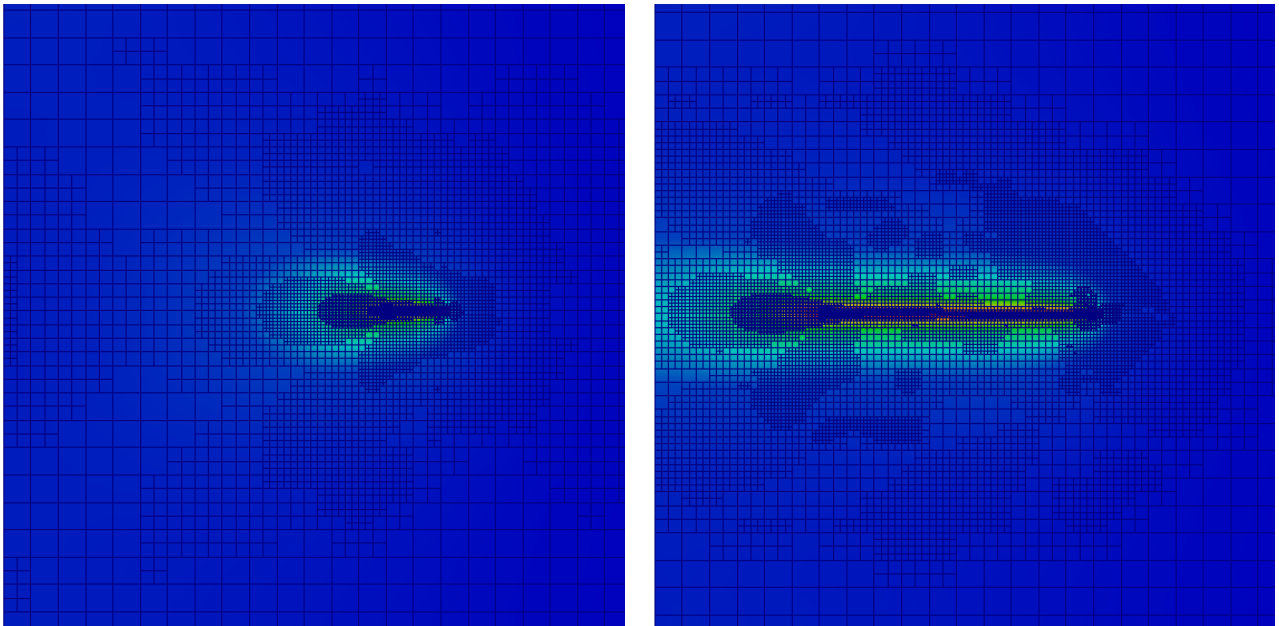


Figure 22: Enhanced extract of the phase-field function after six refinement steps in certain time steps (after 0.00615 and 0.00635 s) for the single edge notched tension test given on the current adaptive mesh.

To improve the transparency of the new developed error estimator and the adaptive refinement strategy regarding the detected error, Figure 22 contains zoomed snapshots of the phase field function and the current adaptive meshes are given at the time steps 615 and 635.

6 Conclusions

The focus of this work was to develop a residual-type error estimator for phase-field fracture propagation problems. Due to the fracture irreversibility constraint, we deal with a variational inequality in time. Based on these theoretical advancements, we developed an adaptive solution strategy for the monolithically-coupled displacement/phase-field system. We investigated the performance by the help of two numerical configurations. First, we considered the so-called single edge notched shear test in which a curved fracture develops. Fixing the phase-field regularization parameter and varying the spatial mesh parameter, we obtained excellent convergence behavior of the load-displacement curves. The same observations were made for the evolution of the bulk and the crack energy. In view of mesh adaptivity, we obtained localized mesh refinement in the (a priori unknown) fracture region. For the second numerical example, the single edge notched tension test, we noticed that here we have very fast, brutal crack growth, which is challenging for mesh refinement strategies. Again, we observed very convincing findings. In ongoing work, we will apply the proposed residual-based error estimator to a phase-field fracture model in incompressible solids. Furthermore, we will provide the proofs of the reliability and efficiency of the proposed estimators, with constants independent of the chosen parameter ϵ .

Acknowledgments

This work has been supported by the German Research Foundation, Priority Program 1748 (DFG SPP 1748) named *Reliable Simulation Techniques in Solid Mechanics. Development of Non-standard Discretization Methods, Mechanical and Mathematical Analysis*. Our subproject within the SPP1748 reads *Structure Preserving Adaptive Enriched Galerkin Methods for Pressure-Driven 3D Fracture Phase-Field Models* (WA 4200/1-1 and WI 4367/2-1 and WO 1936/5-1).

References

- [1] M. Ambati, T. Gerasimov, and L. De Lorenzis. A review on phase-field models of brittle fracture and a new fast hybrid formulation. *Computational Mechanics*, 55(2):383–405, 2015.
- [2] L. Ambrosio and V. Tortorelli. On the approximation of free discontinuity problems. *Unione Matematica Italiana. Bollettino. B. Serie VII*, 6(1):105–123, 1992.
- [3] L. Ambrosio and V. M. Tortorelli. Approximation of functional depending on jumps by elliptic functional via Γ -convergence. *Communications on Pure and Applied Mathematics*, 43(8):999–1036, 1990.

- [4] D. Arndt, W. Bangerth, D. Davydov, T. Heister, L. Heltai, M. Kronbichler, M. Maier, J.-P. Pelteret, B. Turcksin, and D. Wells. The deal.II library, version 8.5. *Journal of Numerical Mathematics*, 25(3):137–145, 2017.
- [5] M. Artina, M. Fornasier, S. Micheletti, and S. Perotto. Anisotropic mesh adaptation for crack detection in brittle materials. *SIAM Journal on Scientific Computing*, 37(4):B633–B659, 2015.
- [6] M. J. Borden, C. V. Verhoosel, M. A. Scott, T. J. R. Hughes, and C. M. Landis. A phase-field description of dynamic brittle fracture. *Computer Methods in Applied Mechanics and Engineering*, 217/220:77–95, 2012.
- [7] S. Burke, C. Ortner, and E. Süli. An adaptive finite element approximation of a variational model of brittle fracture. *SIAM Journal on Numerical Analysis*, 48(3):980–1012, 2010.
- [8] Z. Chen and R. Nochetto. Residual type a posteriori error estimates for elliptic obstacle problems. *Numerische Mathematik*, 84(4):527–548, 2000.
- [9] T. A. Davis. Algorithm 832: UMFPACK V4. 3—an unsymmetric-pattern multifrontal method. *ACM Transactions on Mathematical Software*, 30(2):196–199, 2004.
- [10] The Differential Equation and Optimization Environment: DOPELIB, 2012–2019.
- [11] G. Francfort and J.-J. Marigo. Revisiting brittle fracture as an energy minimization problem. *Journal of the Mechanics and Physics of Solids*, 46(8):1319–1342, 1998.
- [12] C. Goll, T. Wick, and W. Wollner. DOpElib: Differential equations and optimization environment; A goal oriented software library for solving PDEs and optimization problems with PDEs. *Archive of Numerical Software*, 5(2):1–14, 2017.
- [13] A. A. Griffith. The phenomena of flow and rupture in solids. *Transactions of the Royal Society of London. Series A*, 221:163–198, 1921.
- [14] T. Gudi and K. Porwal. A posteriori error control of discontinuous Galerkin methods for elliptic obstacle problems. *Mathematics of Computation*, 83(286):579–602, 2014.
- [15] T. Gudi and K. Porwal. A posteriori error estimates of discontinuous Galerkin methods for the Signorini problem. *Journal of Computational and Applied Mathematics*, 292:257–278, 2016.
- [16] T. Heister, M. F. Wheeler, and T. Wick. A primal-dual active set method and predictor-corrector mesh adaptivity for computing fracture propagation using a phase-field approach. *Computer Methods in Applied Mechanics and Engineering*, 290:466–495, 2015.
- [17] T. Heister and T. Wick. Parallel solution, adaptivity, computational convergence, and open-source code of 2d and 3d pressurized phase-field fracture problems. *PAMM*, 18(1):e201800353, 2018.
- [18] P. Hild and S. Nicaise. Residual a posteriori error estimators for contact problems in elasticity. *M2AN. Mathematical Modelling and Numerical Analysis*, 41(5):897–923, 2007.

- [19] M. Hintermüller, K. Ito, and K. Kunisch. The primal-dual active set strategy as a semismooth Newton method. *SIAM Journal on Optimization*, 13(3):865–888, 2003.
- [20] K. Ito and K. Kunisch. *Lagrange multiplier approach to variational problems and applications*, volume 15 of *Advances in Design and Control*. Society for Industrial and Applied Mathematics (SIAM), Philadelphia, PA, 2008.
- [21] N. Kikuchi and J. T. Oden. *Contact problems in elasticity: A study of variational inequalities and finite element methods*, volume 8 of *SIAM Studies in Applied Mathematics*. Society for Industrial and Applied Mathematics (SIAM), Philadelphia, PA, 1988.
- [22] R. Krause, A. Veese, and M. Walloth. An efficient and reliable residual-type a posteriori error estimator for the Signorini problem. *Numerische Mathematik*, 130(1):151–197, 2015.
- [23] S. Lee, M. F. Wheeler, and T. Wick. Pressure and fluid-driven fracture propagation in porous media using an adaptive finite element phase field model. *Computer Methods in Applied Mechanics and Engineering*, 305:111–132, 2016.
- [24] C. Miehe, M. Hofacker, and F. Welschinger. A phase field model for rate-independent crack propagation: Robust algorithmic implementation based on operator splits. *Computer Methods in Applied Mechanics and Engineering*, 199(45-48):2765–2778, 2010.
- [25] C. Miehe, F. Welschinger, and M. Hofacker. Thermodynamically consistent phase-field models of fracture: variational principles and multi-field fe implementations. *International Journal for Numerical Methods in Engineering*, 83(10):1273–1311, 2010.
- [26] K.-S. Moon, R. H. Nochetto, T. von Petersdorff, and C.-S. Zhang. A posteriori error analysis for parabolic variational inequalities. *M2AN. Mathematical Modelling and Numerical Analysis*, 41(3):485–511, 2007.
- [27] R. Nochetto, K. Siebert, and A. Veese. Fully localized a posteriori error estimators and barrier sets for contact problems. *SIAM Journal on Numerical Analysis*, 42(5):2118–2135, 2005.
- [28] T. Richter. *Parallel multigrid method for adaptive finite elements with application to 3D flow problems*. PhD thesis, Mathematisch-Naturwissenschaftliche Gesamtfakultät, Universität Heidelberg, 2005.
- [29] R. T. Rockafellar. Lagrange multipliers and optimality. *SIAM Review*, 35(2):183–238, 1993.
- [30] J.-F. Rodrigues. *Obstacle problems in mathematical physics*, volume 134 of *North-Holland Mathematics Studies*. North-Holland Publishing Co., 1987. Notas de Matemática [Mathematical Notes], 114.
- [31] A. Veese. Efficient and reliable a posteriori error estimators for elliptic obstacle problems. *SIAM Journal on Numerical Analysis*, 39(1):146–167, 2001.

- [32] R. Verfürth. A review of a posteriori error estimation techniques for elasticity problems. *Computer Methods in Applied Mechanics and Engineering*, 176(1-4):419–440, 1999.
- [33] B. Vexler and W. Wollner. Adaptive finite elements for elliptic optimization problems with control constraints. *SIAM Journal on Control and Optimization*, 47(1):509–534, 2008.
- [34] M. Walloth. Residual-type a posteriori estimator for a quasi-static Signorini contact problem. Technical Report Preprint 2721, Fachbereich Mathematik, TU Darmstadt, 2018.
- [35] M. Walloth. Residual-type a posteriori estimators for a singularly perturbed reaction-diffusion variational inequality – reliability, efficiency and robustness. Technical Report 1812.01957, arXiv, 2018.
- [36] M. Walloth. A reliable, efficient and localized error estimator for a discontinuous Galerkin method for the Signorini problem. *Applied Numerical Mathematics*, 135:276–296, 2019.
- [37] A. Weiss and B. I. Wohlmuth. A posteriori error estimator and error control for contact problems. *Mathematics of Computation*, 78(267):1237–1267, 2009.
- [38] A. Weiss and B. I. Wohlmuth. A posteriori error estimator for obstacle problems. *SIAM Journal of Scientific Computing*, 32(5):2627–2658, 2010.
- [39] T. Wick. Goal functional evaluations for phase-field fracture using PU-based DWR mesh adaptivity. *Computational Mechanics*, 57(6):1017–1035, 2016.
- [40] T. Wick. An error-oriented Newton/inexact augmented Lagrangian approach for fully monolithic phase-field fracture propagation. *SIAM Journal on Scientific Computing*, 39(4):B589–B617, 2017.
- [41] T. Wick. Modified Newton methods for solving fully monolithic phase-field quasi-static brittle fracture propagation. *Computer Methods in Applied Mechanics and Engineering*, 325:577–611, 2017.
- [42] Q. Zou, A. Veese, R. Kornhuber, and C. Gräser. Hierarchical error estimates for the energy functional in obstacle problems. *Numerische Mathematik*, 117(4):653–677, 2011.